UCLouvain

École polytechnique de Louvain

Towards an agile Power-to-Ammonia pathway:

Optimization of a dynamic ammonia production process

Author: **Kamyll Dawn Cocon**
Supervisors: **Francesco Contino, Kevin Verleysen**
Reader: **Juray De Wilde**
Academic year 2020–2021
Master [120] in Chemical and Materials Engineering

Contents

Abstract

The intermittent nature of renewable energies had made its high penetration ($\geq$ 15%) in the grid difficult unless upgrades are made to increase the grid's flexibility. However, this need can be circumvented by storing the excess energy in ammonia and re-injecting this energy back to the grid during shortage. This storage concept, called power-to-ammonia, relies on renewable energies to power the electrolyzer which produces the H_2 needed for the Haber-Bosch synthesis process. Nevertheless, the variability of the electric supply causes fluctuations in the H_2 supply to the synthesis loop, which is not optimized for flexible operation. These fluctuations can cause temperature to vary inside the reactor such that limit cycle behavior or temperature extinction is achieved, resulting to catalyst disintegration. Therefore, a reactor system designed to have high temperature resilience is of great interest. Using Non-dominated Sorting Genetic Algorithm-II (NSGA-II), deterministic design optimization was performed with the goal of maximizing temperature resilience and NH_3 output flow rate. The Polynomial Chaos Expansion (PCE) was then used to propagate the uncertainties in the model, where robust design optimization was performed on the most resilient deterministic design, to have a reliable net NH_3 output flow rate. The effect of cooling system configuration and reactor volume on temperature resilience was determined by considering a non-optimized volume of the system for the former, while optimizing the volume for maximum resilience and flow rate, for the later. Results showed that introduction of the feed in smaller amounts as quench streams into the reactor system, as in direct quenching, led to slightly higher resilience ($\geq$ 1.01 times) compared to when introducing a single, larger feed, as in indirect quenching. On the other hand, the effect of reactor volume depended on the cooling configuration adopted by the reactor system. The presence of uncertainties led to reactor extinction when using the lowest uncertainty values, while higher steady-state temperature values were obtained under operation at the highest values of uncertainties. Finally, the RDO showed that for the adopted lowest H_2/N_2 ratio during ramping, optimization was unsuccessful. Therefore, improvements need to be made to account for ramping duration during robust optimization.

Chapter 1

Introduction

The issue of global warming and depleting energy resources are not new. In fact, for over 50 years, 145 countries around the world had set policies to support the shift towards renewable energy resources as one of the ways to mitigate global warming [1]. Countries from the European Union (EU) are notable leaders in this endeavor. In Germany and Denmark, it is targeted that 80% and 100% of its energy will be be derived from renewable energies by 2035 [1], respectively. However, increasing the integration of renewable energy in the grid system posses great challenge in terms of balancing the energy supply and demand. This is because for certain renewable energies such as solar and wind, they are non-dispatchable [2] and thus energy is not always readily available to meet consumer needs. As a result, a highly flexible grid is needed.

One way to circumvent around the need for flexible grid is to use energy storage systems. This approach can be carried out in two pathways: the Power-to-X (P2X) and the X-to-Power (X2P) pathways, where "X" refers to the energy storage medium. In P2X, excess energy is stored in "X". During a power shortage, the energy stored in "X" is re-introduced into the grid through the X2P pathway. This thesis focuses on the P2X pathway, in particular, using NH_3 as an energy carrier (i.e. Power-to-Ammonia).

Chapter 2

Power-to-Ammonia

2.1 Renewable energy integration

Global warming occurs when greenhouse gases such as carbon dioxide trap radiation from the sun within Earth, causing the planet to heat up. This warming causes climate change which leads to frequent and extreme weather events, hotter temperatures, and wildlife extinction [3], to name a few. In EU, more than 75% of its greenhouse gas emissions is attributed to the energy sector [4]. Efforts in reducing these emissions are carried out by shifting towards the use of renewable energies [5]. Therefore, increasing the integration of renewable energies in the grid is important to mitigate global warming.

However, a fundamental challenge lies in increasing the integration of renewable energies in the grid at high levels ($\geq$ 15% energy [2]). On the one hand, the transport of electricity from one point (i.e. the energy source) to another (i.e. the end-user) through the grid is done on a per-second basis [6]. This means that matching needs to be continuously done by the operator to reduce stress on the grid [7]. On the other hand, renewable energies such as solar and wind are available based on meteorological conditions and/or time of the day. Therefore, matching between the supply and demand proves to be challenging [7], such that when considering integration at high levels, the flexibility of the grid needs to be increased [8].

A flexible grid refers to a grid system that can respond rapidly according to variations in energy supply and demand [9]. There are different methods to increase grid flexibility such as highly interconnected grid designs, demand-side management and the use of energy storage systems [10]. Increasing grid connectivity allows improvement in the power quality of renewable energies by drawing from multiple, different locations [2, 10]. This improvement eases the matching between the supply and the demand, thereby increasing the flexibility of the grid. With the demand-side management, constraining the demand according to the available energy minimizes the mismatch between the supply and demand, thus reducing the strain on the grid [1]. Finally, energy storage systems can be used to store excess energy during surplus and re-introduce this energy back to the grid during deficit [11]. When considering high penetration of renewable energies, the variability in the energy supply at a larger scale will become more complicated such that increasing the grid interconnectivity and demand-side management will not be enough. Because large amounts of energy can be stored with certain types of energy storage systems, it is a robust way of increasing grid flexibility in the future.

2.2 Ammonia as an energy storage system

The technologies used for energy storage can be grouped into chemical, thermal, electrochemical, mechanical and electrical technologies [12]. Depending on the technology, different amounts of power can be stored for different periods of time. For the purpose of increasing renewable energy penetration in the grid, the ability to store large amounts of power for long duration are important. The chemical storage technology is shown to have the largest storage capacities (100 kW to 1000 MW) for the longest duration of time (hours to weeks) [13]. Next to this, pumped hydro, which is a mechanical type of storage, can store 100 MW to 1000 MW for days, while thermo-mechanical technology such as compressed air energy storage can store 10 MW to 100 MW for the same duration [13]. However, both mechanical and thermo-mechanical technology are limited by its geographic/geological requirements [12], and therefore the chemical storage technology presents a viable option for practical energy storage in the near future.

When choosing the type of chemical storage technology, an important parameter to consider is the energy density. Substances with higher energy density is needed as larger amounts of energy can be stored per unit mass (gravimetric energy density) or per unit volume (volumetric energy density). There are two main types of chemical storage technology considered to be viable for renewable energy storage: the hydrogen and its derivatives, and the hydrocarbons [12]. H_2 possesses the highest gravimetric density among the chemical storage systems (120 MJ/kg LHV [6]), while the hydrocarbons have energy densities which are at least two times lower than H_2 (20-50 MJ/kg LHV [6]). Because hydrocarbons contain carbon in their structure, CO_2 is emitted to the atmosphere upon its use. As such, H_2 had been the popular choice as chemical storage system [14]. Despite having the highest gravimetric energy density and being carbon free, H_2 faces major drawbacks in terms of storage. H_2 is typically stored either in compressed gas or condensed liquid form to facilitate storage and transport. Storage of H_2 in its compressed gas form requires pressures of at least 350 bar at ambient temperatures, while storage in condensed liquid form requires ambient pressures at temperatures of around -254 °C [6]. Thus, the extreme conditions needed for H_2 storage makes the process complicated, requiring special storage vessels which are expensive [6]. Because of this, non-carbon containing H_2 derivatives had been sought after as an alternative.

NH_3 is an attractive alternative to H_2 as an energy storage due to its comparable volumetric energy density, relatively easier and cheaper storage, mature distribution system and thorough knowledge in handling and safety. NH_3 contains one of the highest gravimetric (17.8%) H_2 densities, and the highest volumetric (0.107 kg H_2/L) H_2 densities among the non-carbon containing H_2 derivatives [12]. This allows NH_3 to have a high volumetric energy density (11.5 MJ/L LHV [6]), which is 43% higher than H_2 (8 MJ/L LHV [6]). In contrast, the gravimetric energy density of NH_3 (18.6 MJ/kg LHV [12]) is 84.5% lower than H_2. Despite NH_3 having a lower gravimetric energy density, it is important to point out that storage of H_2 in condensed liquid form requires extreme conditions (-254 °C). On the other hand, the storage of NH_3 in compressed gas form requires a pressure of 10 bar at ambient temperature, while storage in condensed liquid form requires -33 °C at ambient pressure [15]. This difference in storage conditions is due to NH_3 (0.769 kg/m^3 at 273.15 K and 1 atm) being 9.18 times heavier compared to H_2 (0.0838 kg/m^3 at 273.15 K and 1 atm). The possibility of storing NH_3 at relatively milder conditions not only makes its storage cheaper, but also increase the storage cost savings with time. To illustrate, for a storage period of 1 day, the difference in storage cost is 0.68 euros/kg H_2 equivalent between NH_3 (0.03 euros/kg H_2 equivalent) and H_2 (0.71 euros/kg H_2 equivalent). For a storage period of 182 days, the difference in storage cost is 12.99 euros/kg H_2 equivalent between NH_3 (0.49 euros/kg H_2 equivalent) and H_2 (13.48 euros/kg H_2 equivalent) [6].

On the other hand, NH_3 has an established distribution system thanks to its century long history of production. As a base chemical for a large number of intermediate products, the demand of NH_3 is high, being the second most produced inorganic chemical next to sulfuric acid [16]. Examples of important products produced from NH_3 are fertilizers, explosives, pharmaceuticals, refrigeration, etc [17]. In the Netherlands, the distribution of NH_3 is done via rail, pipes, ships, or even via its own transportation line (Betuwe line) [6]. With such demand of NH_3, there exist extensive knowledge in terms of its handling and storage. In fact, numerous classification and labelling systems for the transport of NH_3 had already been defined by the United Nations and are currently being used [15]. Even though NH_3 is classified as a toxic gas by the United Nations, it is detectable at low concentrations (20-50 ppm) due to its pungent smell [12]. Health effects in the form of severe irritation with no lasting effect on short term exposure (15 minutes) is only experienced at concentrations of at least 400 ppm [18]. Therefore, through its carbon-free structure, comparable volumetric energy density, relatively milder storage conditions, mature distribution system and knowledge in storage and handling, NH_3 offers the best chemical storage system for renewable energies.

2.3 Power-to-Ammonia technology

The increase of renewable energy integration in the grid through the use of NH_3 can be done through the power-to-ammonia technology (Figure 2.1). This technology is mainly comprised of a H_2 production unit, a N_2 production unit, and an NH_3 production unit. Renewable energies are used to power the electrolyzer, which split water (H_2O) into H_2 and O_2. The resulting stream, which consists of a mixture of H_2, O_2 and H_2O, then proceeds to a separation unit where H_2 is isolated. On the other hand, N_2 is extracted from air through separation processes such cryogenic distillation, pressure swing swing adsorption, and vacuum swing adsorption, or through the use membrane technologies such as polymeric membranes and ceramic membranes [15]. The resulting H_2 and N_2 streams then undergoes compression, where it enters the NH_3 synthesis unit to produce NH_3.

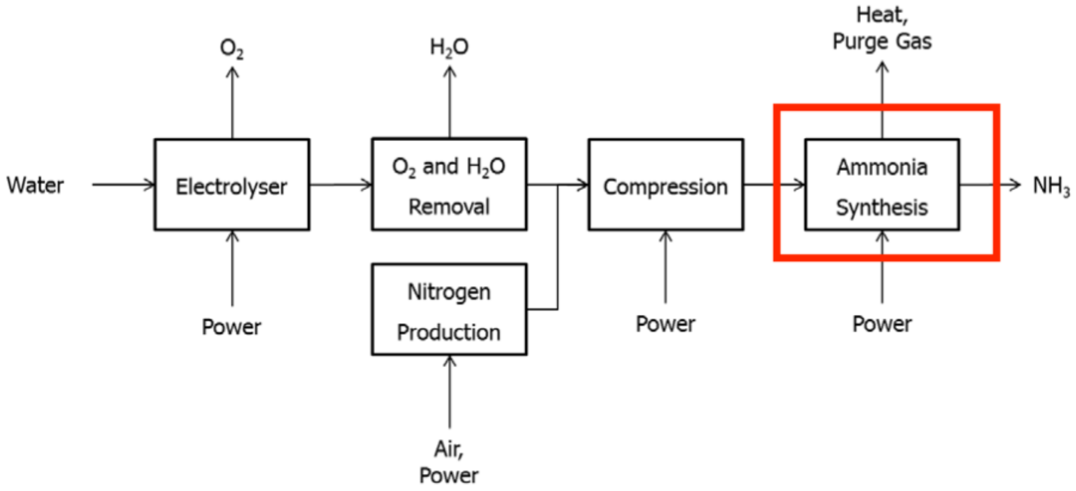

Figure 2.1: The power-to-ammonia technology consists mainly of a H_2 production unit, a N_2 production unit and an NH_3 production unit. The focus of this thesis is the ammonia synthesis unit, highlighted by the red box. Modified from [15].

The fast response time of electrolyzers make it compatible with the renewable energy. For Proton Exchange Membrane (PEM) and alkaline electrolyzers, both have response times in the order of milliseconds [19]. This fast response time allows the electrolyzer to have flexible operation which is necessary when dealing with the intermittency of the renewable energies. However, this is not always the case for the NH_3 synthesis unit. The fluctuations in the energy input result to varying amounts of H_2 fed to the synthesis unit. For certain synthesis units such as the Haber-Bosch synthesis (HBS) loop, flexible operation was not considered in its initial design [20]. As such, at certain amounts of H_2 input, the system may undergo reactor extinction or run-away. Therefore, optimization of the NH_3 synthesis unit for flexible operation is important, which is the purpose of this thesis.

In what follows, the alternative technologies for NH_3 synthesis will be discussed, starting with the HBS loop, followed by electrochemical synthesis, non-thermal plasma, and finally photocatalysis. After the introduction of each technology, comparison will be done to identify the best NH_3 synthesis technology for power-to-ammonia application.

2.3.1 Haber-Bosch synthesis

The HBS process is one of the most important industrial process developed. It is currently the main process used for NH_3 production, responsible for at least 90% of the production in 2018 [21]. This is important because about 80% of the NH_3 is used for the production of fertilizers [17]. Without it, the world would have been 4 billion people short in 2018 [22]. Essentially, there are 3 main steps comprising the HBS process : feed preparation, reaction, and separation (Figure 2.2). During feed preparation, N_2 from air and H_2 from the steam methane reforming process are compressed and heated to reach the desired reaction conditions (400–500 °C and 150–300 bar) [21, 23–25]. As previously mentioned, the separation of N_2 from air is typically done through cryogenic distillation [21, 26] or pressure swing adsorption [11, 21, 25].

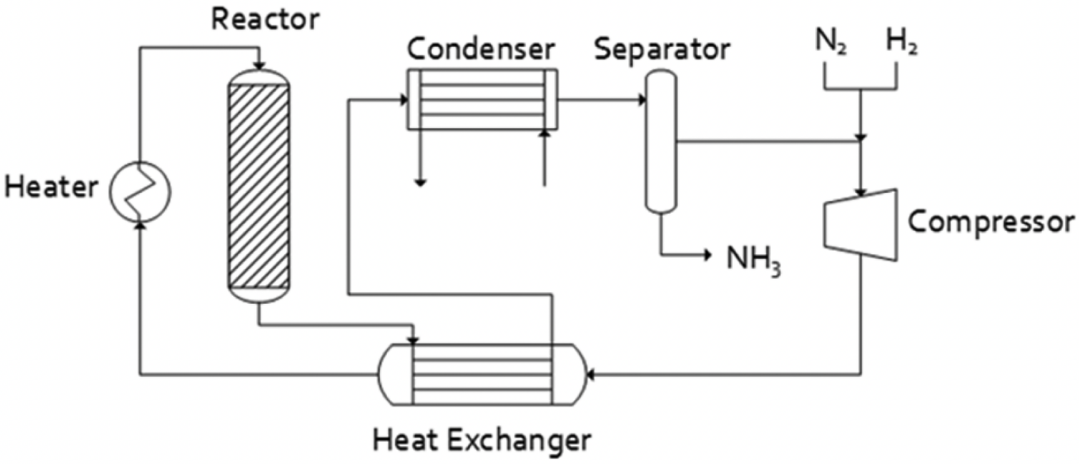

Figure 2.2: The Haber-Bosch synthesis is mainly comprised of three steps: feed preparation, reaction, and separation. of inerts is not shown in this diagram for simplicity [27].

During reaction, 1 mole of N_2 and 3 moles of H_2 are reacted to produce 2 moles of NH_3, as shown:

$$N_{2(g)} + 3\,H_{2(g)} \rightleftarrows 2\,NH_{3(g)} \quad \Delta H_f^{\circ} = -45.90\,\mathrm{kJ/mol_{NH_3}} \tag{2.1}$$

This exothermic, equilibrium reaction is carried out in the presence of catalyst at 400–500 °C and 150–300 bar [21, 23–25]. The catalyst used for NH_3 production is typically iron-based, specifically the wustite or magnetite-based [24, 26], although ruthenium-based catalysts are also used under milder conditions (280–450 °C and 9.9 bar) [28]. To explain this need for extreme reaction conditions, it is important to first discuss the mechanism of NH_3 production via HBS.

There are three mechanisms used to describe the production of NH_3 from H_2 and N_2: the dissociative pathway, the associative alternating pathway and the associative distal pathway [29]. Among the three mechanisms mentioned, the dissociative pathway is the widely accepted mechanism of NH_3 production via HBS [29, 30]. According to this mechanism (Figure 2.3), the N_2 first undergo dissociation by forming a bond with the surface of the catalyst. Once bonded, the resulting nitride then undergoes a step-by-step hydrogenation, releasing NH_3 at the last step. As N_2 is a very stable molecule, the process of dissociating N_2 requires 941 kJ/mol N_2 for all three bonds [31], making this step the rate determining step of the reaction. Therefore, for NH_3 to be produced, high temperature (400–500 °C) is employed to attain sufficient kinetic activity [21]. On the other hand, since NH_3 production is exothermic ($\Delta H_f^{\circ} = -45.90\,\mathrm{kJ/mol_{NH_3}}$), the high temperature causes the equilibrium reaction to not favor NH_3 production. Because of this, high pressure (150–300 bar) is employed to force the equilibrium to favor NH_3 production.

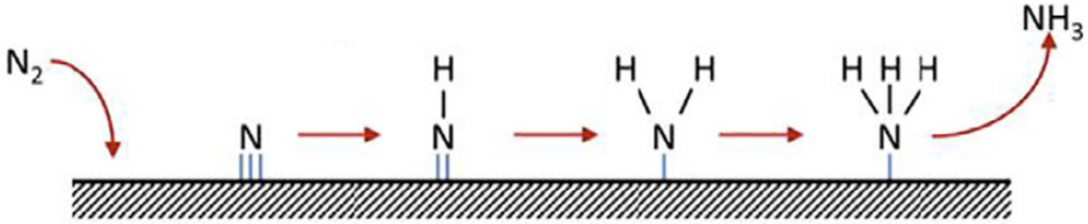

Figure 2.3: The dissociative pathway mechanism for NH_3 production via HBS involves two things: dissociation of N_2 and hydrogenation of H_2. The dissociation of N_2 is the rate determining step of the reaction. Diagram taken from [29].

The interplay between the reaction kinetics and thermodynamic equilibrium makes temperature an important design parameter for the HBS. On the one hand, high temperature is needed for faster kinetics, while on the other hand, the thermodynamic equilibrium of NH_3 production is favored at low temperature. Generally speaking, there are 2 types of reactor systems used for NH_3 synthesis: the tubular and multi-bed reactor systems [20, 32]. The difference between the two lies with the temperature control management. For tubular reactors, cooling is achieved through the use of cooling medium which is at indirect contact with the catalyst. This cooling medium can either be situation inside the reactor with the catalyst outside, or vice versa [20]. The continuous contact between the cooling medium and catalyst allows the best temperature profile for maximum NH_3 production to be achieved [32] while allowing efficient heat recovery [20, 32] for tubular reactors. Multi-bed systems on the other hand, is cooled either by direct or indirect quenching between the catalyst beds [20, 33]. This bed-wise cooling makes the temperature control discontinuous resulting to temperature profiles which does not always correspond to maximum NH_3 production [32]. Nevertheless, tube cooled systems are at least three times more expensive than the multi-bed systems [20]. Furthermore, numerous literature [20, 33] and industries [34, 35] had pointed to the use of 3-bed adiabatic indirect quenched reactor as the best balance in terms of cost and performance.

The single pass conversion of HBS is 15% [24] and therefore after the reaction, the outlet stream still contains a significant amount of H_2 and N_2, along with NH_3. Because of this, recycling is done resulting to an overall conversion of 97% [21]. To avoid accumulation of NH_3 in the recycle stream, the reactor outlet stream undergoes a separation process prior to recycling. This is important as large amounts of NH_3 in the reactor will result to its consumption to produce N_2 and

H_2 (reverse reaction of Equation 2.1). Cryogenic separation at -20 °C [20, 36] is the most common method of separating NH_3 [25] which takes advantage of the different condensation temperatures of the components in the mixture. Because NH_3 is the heaviest among the mixture, it will be condensed first and the light components such as N_2, H_2 and inerts can then proceed to recycling with a portion of it purged.

2.3.2 Alternative ways of ammonia production

The need for extreme conditions makes HBS an energetically intensive process requiring at least 600 kJ/mol NH_3 [37, 38]. Alternative ways of NH_3 production had been developed over the past years to allow NH_3 production at relatively milder conditions, ideally at ambient conditions. As discussed previously, the conflict between reaction kinetics and thermal equilibrium resulted to the need for high temperature and pressure operation in HBS for maximum NH_3 production. To operate at relatively milder conditions, the reaction kinetics can be increased while removing the influence of thermal equilibrium [39], as will be discussed. There are currently numerous alternative NH_3 production methods being studied however, focus will be given on the electrochemical process, the non-thermal plasma and the photocatalysis.

Electrochemical synthesis

The electrochemical process produces NH_3 directly from N_2 (air) and H_2 or H_2O via redox reactions [17, 39–41]. The process uses an electrolytic cell which is composed of an anode on one side and a cathode on the other side (figure 2.4). The electrodes are separated by an electrolyte which can be of different types. Depending on the electrolyte involved, the substance introduced to each electrodes slightly varies. Generally speaking, H_2 containing compounds such as H_2O or hydrocarbon fuel is fed at the anode side and N_2 either alone or in the presence of H_2O is fed at the cathode side [42]. During production, electrons are generated from the oxidation of H_2 or H_2O in the anode and then consumed for the reduction of N_2 to NH_3 in the cathode. Ions can also be liberated from the redox reactions which will diffuse through the electrolyte to participate in the reaction. Because of the separation of the reactants by the electrolyte, the effect of equilibrium on the reaction is removed [39]. How fast the reaction will proceed then depends on how fast the electrons or ions diffuse through the electrolyte to reach the appropriate electrode for reaction [39].

The different electrolytes used for NH_3 production are: solid, molten and aqueous electrolytes (figure 2.4). The electrochemical process that uses solid electrolytes are commonly referred as solid-state electrochemical ammonia synthesis (SSAS) [39]. This solid electrolytes are dense, acting as barrier for gas diffusion and facilitating the transfer of proton (proton SSAS) or oxide ions (O_2- SSAS) [17, 39]. SSAS uses porous electrodes and is operated at high temperatures ($T > 500\,°C$) [17, 21, 39, 42]. On the other hand, molten electrolytes uses molten metal salts which allow ionic conductivity to be increased [39]. The increase in ionic conductivity allows operation at intermediate temperatures ($100\,°C < T < 500\,°C$) [17, 21, 39, 42] to be possible. Finally, in an effort to produce NH_3 at ambient conditions, aqueous electrolytes were developed which can be operated at low temperatures ($T< 100\,°C$) [39, 42].

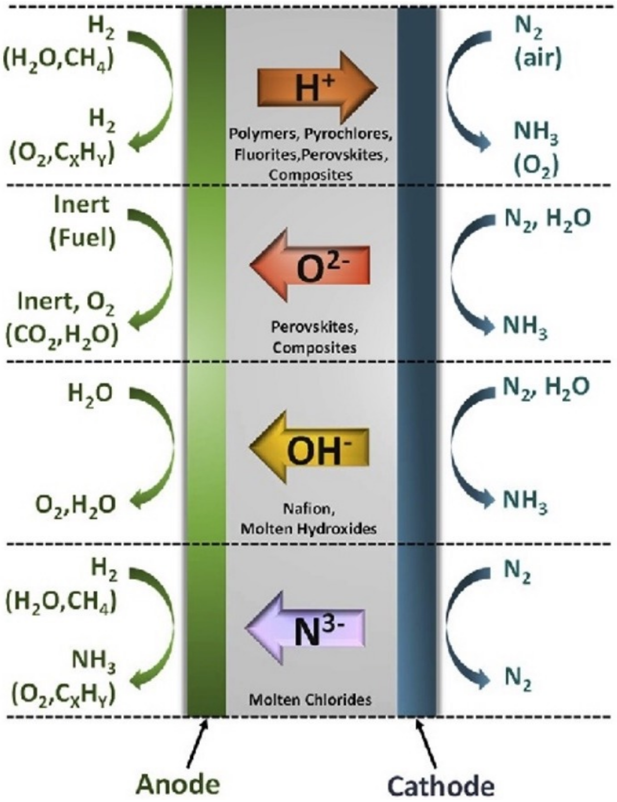

Figure 2.4: Diagram depicting the most commonly used design for electrochemical NH_3 synthesis [42].

Non-thermal plasma

The first industrial plasma-based N_2 fixation was developed before the HBS in 1903 by Birkeland and Eyde which utilized thermal arc furnace to convert air into nitrogen oxides (NOx) [43, 44]. However, it suffered low NOx yield and low energy efficiency and thus was eventually replaced by HBS as an alternative N_2 fixation technique [45]. Since then, the use of plasma for N_2 fixation had been continuously studied. In non-thermal plasma (NTP), only the electrons (contrary to thermal plasma) are at high temperatures (several 10^5 K). The rest of the species such as the gas molecules and ions are at around ambient temperature [45–47]. The idea is to use the highly energetic electrons to excite, ionize and dissociate the gas molecules which will then react further [45, 46]. In this way, the energy needed is only for the heating up of the electrons and operation at atmospheric pressure is possible [45, 48]. Depending on the type of plasma generated, the energy requirement for the excited electrons varies. In terms of NH_3 production, the dielectric barrier discharge is commonly chosen due to the possibility of catalyst inclusion in the reactor [49]. Indeed, plasma is non-selective thus the presence of catalyst will increase selectivity for NH_3 production [45]. The dielectric barrier discharge reactor (figure 2.5) is composed of 2 electrodes, one connected to the power supply and the other one grounded. An alternating potential difference is placed between the electrodes. A dielectric barrier is placed between the electrodes to control the electrical current that passes between the electrodes and thus preventing it from becoming thermal plasma. N_2 and H_2 enters from one side of the electrode and react as it travels through the reactor. The formed NH_3 then exits at the other electrode. The main parameter for the process is the strength of the electric field which can be controlled through the distance between the electrodes and the applied voltage frequency [46]. Optimum values for voltage frequency is taken to be 1 kHz to 10 MHz [50]. Catalyst can be incorporated in the reactor region to provide selectivity of the reaction [49].

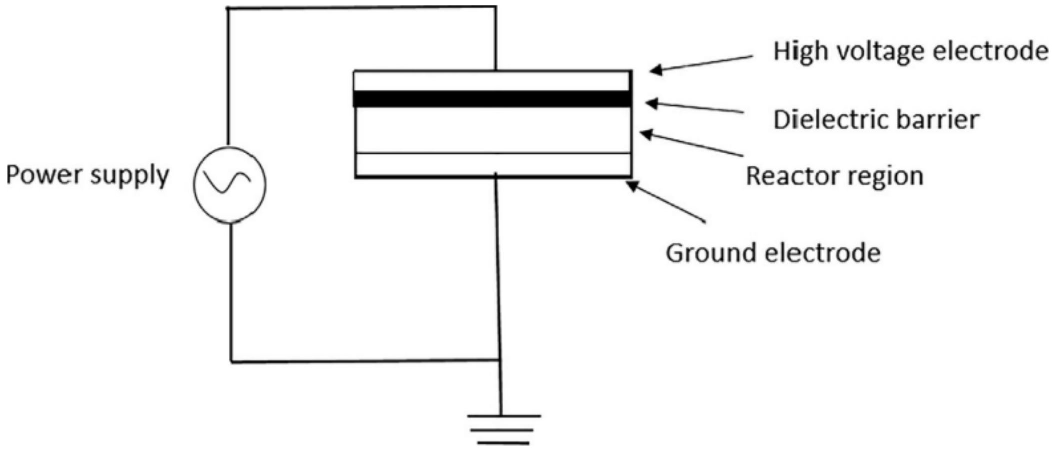

Figure 2.5: Schematic diagram of dielectric barrier discharge reactor. The catalyst (not shown here) can be placed in the reactor region to increase the selectivity of the reaction [46].

Photocatalysis

Photocatalysis is another promising alternative technology for producing NH_3 in ambient conditions using only abundant, cheap substances, N_2, H_2O and sunlight. The process makes use of semiconducting photocatalysts which absorb photons of the right energy to perform charge carrier separation [51–53]. In this phenomenon, the electrons are excited from the valence band (VB) to the conduction band (CB), generating holes along the process. The holes will cause oxidation of the H_2O to H^+ ions whereas the electron and the H^+ ions will be used by the N_2 for its reduction into NH_3 at the surface (figure 2.6).

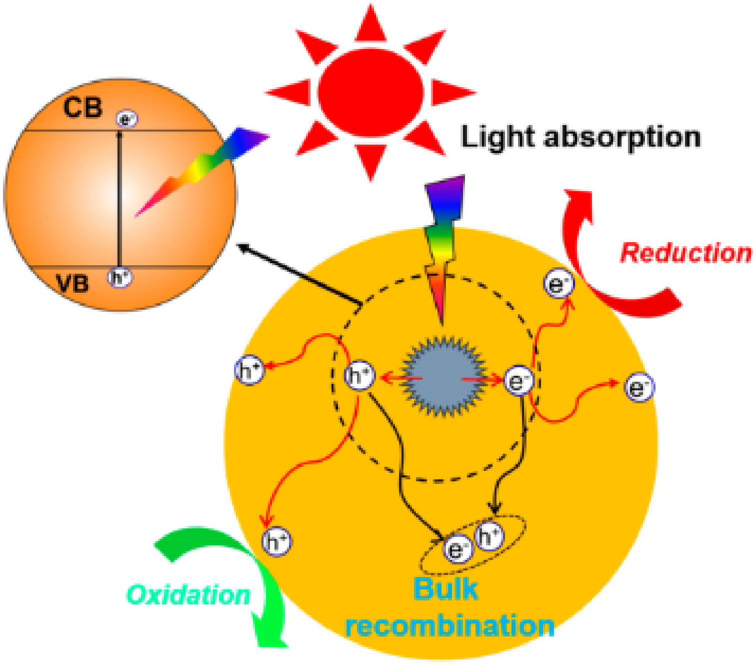

Figure 2.6: Mechanism of NH_3 production via photocatalysis [53].

Examples of semiconducting photocatalysts studied are TiO_2, Fe_2O_3, WO_3, ZnO and Ga_2O_3 [52]. Timeline of the catalyst development can be seen in the review article of Zhang et al. [52]. Despite the promise of this technology, it is still far from industrial application. Major challenges experienced by this technology is ineffective light absorption which can be attributed to a large band gap between the VB and CB as well as fast electron-hole recombination process [53]. To address this, suggestions are made such as introduction of metal active sites to provide more active centers, as well as introduction of noble metals such as Pt, Ru, Pd, Rh into the photocatalyst to act as electron acceptors to promote charge carrier separation and suppress electron hole recombination [53]. Although this technology is still at its early stages [52], the potential of harnessing sunlight to drive the reaction which requires extreme conditions in industrial setting makes it worth mentioning.

2.3.3 Comparison

In this section, comparison is made between the HBS and the 3 alternative NH_3 production technologies: electrochemical synthesis, non-thermal plasma and photocatalysis. It is important to note that comparison is difficult mainly due to the lack of common performance indicators between the considered technologies.

Nevertheless, 3 criteria is used to assess the suitability of the technology for P2A process: energy efficiency, NH_3 yield and TRL.

The purpose of using P2A technology is to increase the renewable energy integration in the grid through the use of NH_3 energy storage system. This allows the dependency of fossil fuels to be reduced while also reducing CO_2 emission. Therefore, it is important for the ammonia production process of P2A to be energy efficient. One of the main strength of HBS that makes it difficult to replace despite its need for extreme processing conditions is its high energy efficiency of 0.1 MJ/mol NH_3 produced [54]. Among the technology explored, only the energy efficiency of NTP is found (1.5 MJ/mol NH_3 [54]). Because of this, in terms of energy efficiency, only the 2 technologies can be compared with NTP being 15 times less efficient than HBS. Although the efficiency of HBS process decreases with production scale [54], the adjusted energy efficiency corresponding to production rate compatible with renewable energy (10 tons/day [54]) is 0.41 MJ/mol NH_3 produced [54], which is still at least three times lower than the energy efficiency of NTP.

In terms of NH_3 yield, the comparison will be made in terms of single pass conversion for HBS and NTP. This is because there is no data available yet for an overall conversion of NTP which accounts for recycling. On the other hand, a different unit for yield is used for electrochemical process due to the nature of process (diffusion-based). In HBS, the single pass conversion is 15% [24] which is at least 1.5 times higher than the highest attained conversion for NTP which is 9% [55]. For the electrochemical process, there is a minimum order of yield that must be met to be considered profitable in an industrial scale which is $10^{-7}\,\mathrm{mol/cm^2\ s}$ [39]. Among the electrochemical process explored, only the SSAS process is able to reach this order [39]. However, the operating temperature of SSAS ($T > 500\,°C$) is higher than the HBS (400-500 °C) making it not suitable for the purpose of P2A technology.

Finally, it is important to mention that the absence of data that would've allowed better comparison between the NH_3 production technologies is mainly due to the alternative NH_3 production technologies still being in their research stage (TRL 1-3 [24]). Thus, even though there were some missing pieces in the comparison among the technologies, the commercial maturity and high energy efficiency of HBS makes it currently the best technology for P2A.

2.4 Summary and Conclusion

In this chapter, the use of energy storage system as a way to increase the penetration of renewable energy in the grid without the need for high grid flexibility was discussed. Among the energy storage systems, the chemical type proved to be more feasible for long term storage (weeks) of high power (100 - 1000 MW). Particularly, NH_3 shows great promise due to its carbon-free structure, high volumetric energy density and commercial maturity. Nevertheless, because of immense energy consumption and carbon footprint of SMR which is used as the main source of H_2 for NH_3 production, the P2A technology offers a renewable pathway that bridges the need for increased renewable energy integration and sustainable energy storage system.

The HBS has been the main choice for producing NH_3 for the past century. Comparison with other alternative NH_3 production technology proves that it also currently the best NH_3 production technology for P2A due to its high energy efficiency, high NH_3 yield and commercial maturity. Particularly, optimization of a currently established and widely implemented technology would make the goal of high renewable energy penetration in the near future be more attainable. Thus, this thesis will focus on the optimization of HBS at small scale production of around 10 tons/day.

Chapter 3

Methodology

Increasing the integration of renewable energies in the grid is crucial to achieve the greenhouse gas emission cut-off policies. However, the variability of renewable energies makes this integration especially challenging. One way to circumvent this is to use power-to-ammonia technology where NH_3 is used as the energy storage system. Nevertheless, the HBS process was not designed for flexible operation, and a steady supply of energy is needed. To satisfy this need, complementary renewable energy sources, such as wind and solar, are combined [56]. Sometimes, electricity from the grid is supplemented to further improve the stability of the input [56]. Even so, the resulting energy profile will not be perfectly constant, but rather fluctuates with time.

The issue with a fluctuating energy source is that the H_2 produced by the electrolyzer will vary. In turn, the H_2 input to the loop will not be constant and therefore, operation at suitable conditions is not always the case. This can bring the system to an unstable state where limit cycle behavior manifest or worse, reactor extinction can occur. Temperature oscillations inside the reactor is undesirable as it causes thermal cycling of the catalyst, leading to deterioration. On the other hand, re-starting the system from extinction requires special start-up procedures [57], adding up to its down-time and hence, loss in NH_3 production. Therefore, a system capable of recovering back to its normal temperature operation after changes in its H_2 input is of great interest for power-to-ammonia applications. In this thesis, such system is said to have high temperature resilience.

The reactor system is considered as the heart of the HBS, and for adiabatic, fixed-bed reactors, two types of inter-bed cooling configuration typically exist, the direct and indirect quenching. Cheema et al. [20] has shown that operational flexibility differs between the two cooling configurations, with the directly quenched system exhibiting higher flexibility compared to the indirectly quenched system.

On the other hand, the temperature dynamics of ammonia production is linked to the mass of catalyst, as seen in the energy balance, with larger mass associated with higher temperature change with time. When combined with ramping in its H_2/N_2 ratio, the amount of catalyst could indirectly influence the capacity of the system to recover. Therefore, the objective of this thesis is two-fold: (1) examine the effect of cooling system on the temperature resilience and (2) examine the effect of reactor volume on the temperature resilience. The Deterministic Design Optimization (DDO) was first carried out to obtain designs which exhibited maximum NH_3 output flow rate and maximum resilience, deterministically. The effects of the cooling system and reactor volume were then examined through these two extreme designs. Due to the inherent sensitivity of the ammonia reactor system [32], the effect of operational and parametric uncertainties on the deterministic designs were then studied by subjecting the designs to worst-case scenarios. The feed temperature to the reactor system and H_2/N_2 ratio were chosen as operational uncertainties, while heat of the reaction and heat capacities of the gas and catalyst were chosen as parametric uncertainties. Finally, a Robust Design Optimization (RDO) was carried out to obtain a robust design which maximizes the net NH_3 output flow rate.

3.1 System design

The system considered in this study is an adiabatic reactor comprised of three-beds. Between each bed, cooling takes place which can either be accomplished through direct quenching or indirect quenching. The effect of cooling configuration on temperature resilience was studied by considering two systems of the same volume with different cooling configurations. These volumes were calculated based on the operating conditions from Gullberg [58]. On the other hand, the effect of reactor volume on resilience was also investigated by optimizing the bed volumes of both configurations for maximum net NH_3 output flow rate and maximum resilience. In this section, the methodology adopted for the system design is detailed. First, the schematic diagram of the two studied reactor systems are presented. Then, the set of equations used to model the reactor bed, heat exchanger and mixer are provided. These equations were solved using GEKKO from Python which is discussed next. Then, the result of the model validation with literature is presented. Finally, the method adopted for calculating the reactor volume used for the first objective is discussed.

3.1.1 System configuration

The reaction governing ammonia synthesis is an equilibrium-based reaction which is exothermic. As the reaction proceeds, heat is generated causing the temperature of the system to rise. By Le Chatelier's principle, removal of some of the generated heat is important to maintain high reaction rate. For fixed-bed reactors used in ammonia synthesis, cooling is popularly done either through direct quenching or indirect quenching. In the directly quenched system, the feed stream is split into smaller fractions which is fed in-between the reactor beds. This cold stream will be introduced into the hot reactor bed directly, resulting to quenching of the temperature and change in gas concentration at the inlet of the bed. Because of this abrupt change in temperature, direct quenching does not allow precise and smooth temperature control, which is important for maintaining close operation at the maximum reaction rate [32]. On the other hand, for indirectly quenched system, a single feed enters the reactor at the top and then heat exchanger(s) are used to cool the outlet stream before proceeding to the next bed. This indirect cooling is achieved through heat exchanger(s) which allows for better temperature control over the inlet temperature of the beds, resulting to operation close to the maximum reaction rate [32].

The reactor system configurations considered in this thesis were adopted from Cheema et al [20]. Both systems are considered as adiabatic and consist of three beds. The inlet stream, at a certain feed pressure P_f and feed molar flow rate n_f, enters at the top (bed 1) and exits at the bottom (bed 3) (Figure 3.1). For the directly quenched system, the feed entering the reactor is split into three quench streams and one inlet stream at the top of reactor bed 1 (V_1). The temperature of the inlet stream T_i is controlled through the use of a valve u_3 and a heat exchanger A_{HX}. As the stream flows through the bed, the heat generated from the reaction causes its temperature to increase. Prior to entering the next bed, the exit stream is cooled down by mixing with the quench stream. The process continues until the final exit stream is cooled by A_{HX}. The same can be said about the indirectly quenched system except that the entire feed enters through V_1, and exits all together at the final bed V_3. On the other hand, autothermal operation for the directly quenched system is attained mainly through the heat balance at A_{HX}, while for the indirectly quenched system, autothermal operation depends on the heat balance on all three heat exchangers.

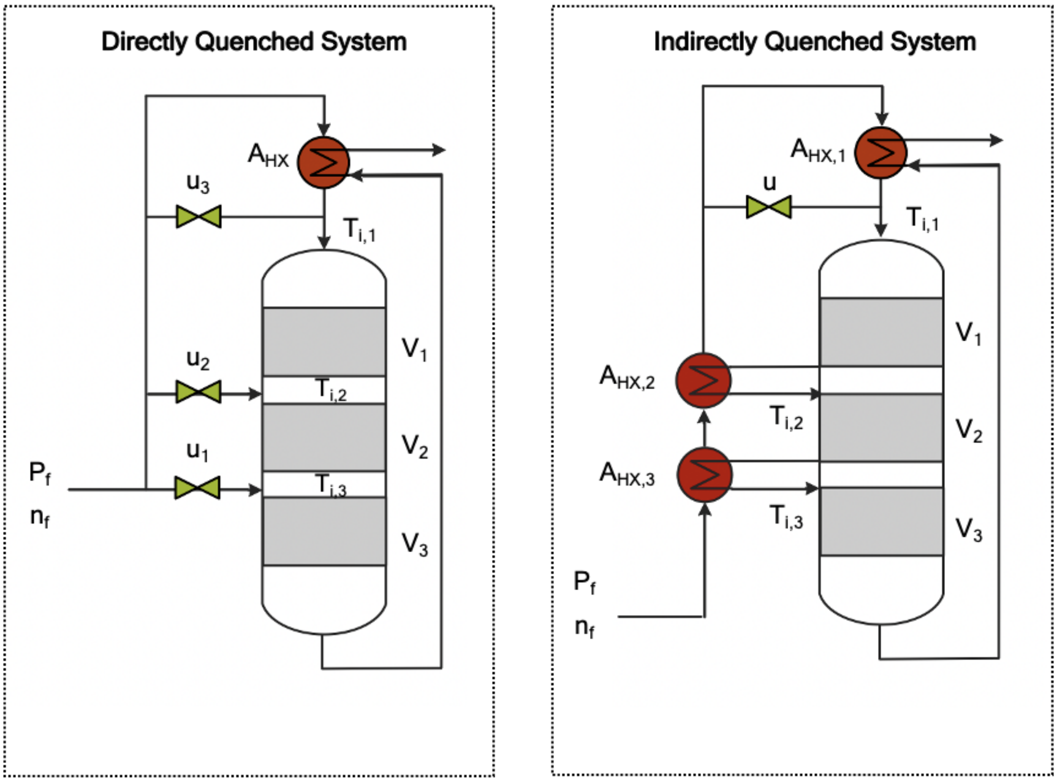

Figure 3.1: The two system configurations studied are the direct (left) and indirectly quenched system (right). These configurations were optimized using the parameters shown.

3.1.2 Reactor bed

There exist different models for modelling a fixed-bed reactor. Broadly speaking, these are the pseudo-homogeneous and heterogeneous models [32]. The main difference between the two is that for the former, no distinction is made between the condition of the gas and solid catalyst, while the later accounts for this difference. These models can be further classified into one-dimensional and two-dimensional modelling where ideal and/or axial mixing is considered in the one-dimensional pseudo-homogeneous model, and interfacial and/or interparticle gradient is considered in the one-dimensional heterogeneous model. On the other hand, the two-dimensional modelling incorporates radial mixing on top of what was just mentioned. In this thesis, a one-dimensional pseudo-homogeneous model was adopted [20, 57, 58]. Furthermore, as the catalyst considered here is a 1.5 to 3 mm size magnetite Fe_3O_4 particles, transport limitations can be neglected [20, 59] due to its small size [59] and high thermal conductivity [60], while pressure drop was considered to be negligible [61].

Performing dynamic modelling on a plug flow system entails numerical resolution of coupled linear or nonlinear partial differential equations [62]. To facilitate the numerical routine, transformation of these partial differential equations to ordinary differential equations are typically done. There are two ways of doing this: the differential reactor approximation, and the staged continuous stirred-tank reactor approximation [62]. In the first method, the partial differential equation is approximated to be equal to its difference quotient ($\partial dy/\partial dx \approx \Delta y/\Delta x$), while the second method approximates the plug flow reactor as a series of continuous stirred-tanked reactors, allowing transformation of the equations to ordinary differential equations using finite differences. This approximation means that the volume can be discretized into volume compartments where perfect mixing occurs (Figure 3.2). In this thesis, the second method is adopted as the first method is only limited to low conversion systems [62]. Finally, the gas hold-up inside the reactor is neglected as it changes at a rate that is much faster than the temperature dynamics [57, 58].

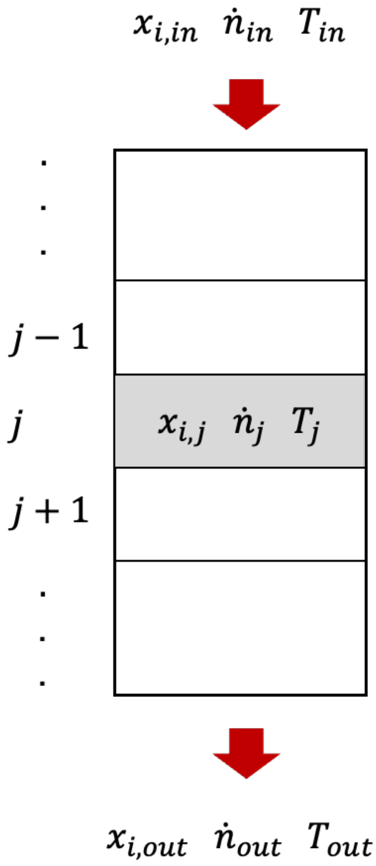

Figure 3.2: The plug flow reactor can be approximated into a series of continuous stirred-tank reactors. This allows transformation of the partial differential equations to ordinary differential equations through finite differences. Diagram modified from [58].

As a summary, the following assumptions were taken to simplify the modelling of the reactor bed.

- Only axial flow
- Negligible pressure drop
- Perfect mixing in each volume compartment
- Negligible gas hold-up
- Constant heat capacity of the gas and catalyst
- Negligible heat capacity of the gas compared to the catalyst

In what follows, equations used to model the reactor beds are presented. These equations are based on performing balance on a single volumetric compartment, thereby allowing the energy balance equation to be expressed as an ordinary differential equation, instead of a partial differential equation.

Mole balance

The mole balance of a system can be generally expressed as

$$\begin{pmatrix}\text{Rate of}\\ \text{moles out}\end{pmatrix} - \begin{pmatrix}\text{Rate of}\\ \text{moles in}\end{pmatrix} = \begin{pmatrix}\text{Rate of moles}\\ \text{accumulated}\end{pmatrix} + \begin{pmatrix}\text{Rate of moles}\\ \text{consumed}\end{pmatrix} \tag{3.1}$$

Considering the j^{th} compartment from Figure 3.2 and neglecting the gas hold-up, the overall mole balance of component i is

$$\dot{n}_j = \dot{n}_{j-1} + \sum_{i}^{species} m_{cat,j} \upsilon_i r_{N_2,j} \tag{3.2}$$

where $\dot{n}$ is the total molar flow rate in kmol/s, r_{N_2} is the rate of N_2 consumption in kmol N_2/kg$_{cat}\cdot$ s, υ_i is the stoichiometric ratio of i, and m_{cat} is the mass of the catalyst inside the volumetric compartment, calculated as

$$m_{cat,j} = \frac{V_{bed}}{nc}\rho_{cat} \tag{3.3}$$

where nc is the number of volume compartments, V_{bed} is the volume of the reactor bed in m^3, and ρ_{cat} is the density of the catalyst in kg/m^3. On the other hand, the component mole balance on the j^{th} compartment is

$$\dot{n}_j x_{i,j} = \dot{n}_{j-1} x_{i,j-1} + m_{cat,j} \upsilon_i r_{N_2,j} \tag{3.4}$$

where x_i is the mole fraction of component i.

Energy balance

Similar to Equation 3.1, the energy balance can be generally expressed as

$$\begin{pmatrix}\text{Rate of}\\ \text{heat out}\end{pmatrix} - \begin{pmatrix}\text{Rate of}\\ \text{heat in}\end{pmatrix} = \begin{pmatrix}\text{Rate of heat}\\ \text{accumulated}\end{pmatrix} + \begin{pmatrix}\text{Rate of heat}\\ \text{consumed}\end{pmatrix} \tag{3.5}$$

The flow stream carries a certain amount of energy which is used for the reaction and/or accumulation within the volumetric compartment. When considering the the j^{th} compartment, the energy balance can be expressed as

$$\frac{\partial T_j}{\partial t} = \frac{C_{p,gas}(\dot{n}_{j-1}T_{j-1} - \dot{n}_j T_j) + m_{cat,j} r_{N_2,j}(-\Delta H_{rx})}{m_{cat,j} C_{p,cat}} \tag{3.6}$$

where T is the temperature in K, ΔH_{rx} is the heat of reaction in J/kmol N_2, and $C_{p,cat}$ and $C_{p,gas}$ are the heat capacity of the catalyst and gas in J/kmol·K, respectively.

Rate of reaction

The kinetic rate expression is based on the Temkin-Pyzhev equation [32] which is expressed in terms of partial pressures, p_i.

$$r_{N_2} = \frac{f}{\rho_{cat}} \left(k_+ p_{N_2} \frac{p_{H_2}^{1.5}}{p_{NH_3}} - k_- \frac{p_{NH_3}}{p_{H_2}^{1.5}} \right) \tag{3.7}$$

where f is the catalyst activity factor, taken to be equal to 4.75 [57], k_+ and k_- are the rate constants for the forward and backward reaction, respectively. In turn, the rate constants can be calculated as

$$k_+ = 1.79 \cdot 10^4 \exp\left(-\frac{87090}{RT}\right) \tag{3.8}$$

$$k_- = 2.57 \cdot 10^{16} \exp\left(-\frac{198464}{RT}\right) \tag{3.9}$$

where R is the gas constant.

3.1.3 Heat exchanger

For the heat exchanger, a steady-state operation was assumed where both the overall heat transfer coefficient and the heat capacity of the gas were taken to be constant during the cooling process. Furthermore, conduction along the tube was not accounted for and the heat exchanger is assumed to be insulated. The method used to model the heat exchanger is the Number of Transfer Units (NTU) method, as it is simpler to use compared to the logarithmitc mean temperature difference method [20]. To start, the heat capacity ratio, C_r is given by

$$C_r = \frac{\dot{n}_{\min} C_{p,gas,\min}}{\dot{n}_{\max} C_{p,gas,\max}} \tag{3.10}$$

where the subscript min and max refers to stream with the minimum and maximum values of C_p, respectively [63]. For the directly quenched system, the minimum and maximum C_p values were identified to be the cold and hot streams, respectively, while the opposite was observed for the indirectly quenched system. On the other hand, the Number of Transfer Units, NTU, is given by

$$NTU = \frac{UA}{\dot{n}_{\min} C_{p,gas,\min}} \tag{3.11}$$

where U is the overall heat transfer coefficient in W/m^2·K, and A is the area of the heat exchanger in m^2. The equation for the effectiveness factor, ϵ, was adopted from Gullberg [58] and is given as

$$\epsilon = \frac{1 - e^{-NTU(1-C_r)}}{1 - C_r e^{-NTU(1-C_r)}} \tag{3.12}$$

The actual heat exchanged per unit time $\dot{Q}$ can then be calculated from ϵ and the maximum possible heat exchanged per unit time, $\dot{Q}_{\max}$ as shown

$$\dot{Q} = \epsilon \dot{Q}_{\max} \tag{3.13}$$

where

$$\dot{Q}_{\max} = \dot{n}_{\min} C_{p,gas,\min}(T_{in,h} - T_{in,c}) \tag{3.14}$$

Finally, the outlet temperatures of the cold and hot streams were calculated as follows

$$\dot{Q} = \dot{n}_h C_{p,gas,h}(T_{in,h} - T_{out,h}) \tag{3.15}$$

$$= \dot{n}_c C_{p,gas,c}(T_{out,c} - T_{in,c}) \tag{3.16}$$

$$T_{out,h} = T_{in,h} - \frac{\dot{Q}}{\dot{n}_h C_{p,gas,h}} \tag{3.17}$$

$$T_{out,c} = T_{in,c} - \frac{\dot{Q}}{\dot{n}_c C_{p,gas,c}} \tag{3.18}$$

3.1.4 Mixer

During mixing, it is assumed that the heat capacity of the streams do not change, and that changes are only associated in terms of temperature and composition. When mixing two streams with inlet temperatures of T_{in1} and T_{in2}, having inlet molar flow rates of n_{in1} and n_{in2}, the outlet temperature of the mixer T_{out}, is given by

$$T_{out} = \frac{\dot{n}_{in1}}{\dot{n}_{in1} + \dot{n}_{in2}} T_{in1} + \frac{\dot{n}_{in2}}{\dot{n}_{in1} + \dot{n}_{in2}} T_{in2} \tag{3.19}$$

Similarly, the outlet mole fraction of component i, $x_{i,out}$ is calculated as

$$x_{i,out} = \frac{\dot{n}_{in1}}{\dot{n}_{in1} + \dot{n}_{in2}} x_{i,in1} + \frac{\dot{n}_{in2}}{\dot{n}_{in1} + \dot{n}_{in2}} x_{i,in2} \tag{3.20}$$

3.1.5 Dynamic simulator tool

The equations previously presented comprises a system of Differential-Algebraic Equations (DAE) which were coded in Python and solved using GEKKO. GEKKO is a Python optimization package developed for solving mixed-integer and DAE. To solve these equations, a GEKKO model is first created by calling the `m.GEKKO` command. Inside this model, Variables, Parameters and Constants are defined and then related through Intermediates and Equations. At the back-end, it uses the Advanced Process Monitor (APMonitor), which is a modelling language for DAE, to compile the model and perform reduction based on the analysis of model's sparsity structure. When specifically dealing with DAE, APMonitor uses orthogonal collocation on finite elements to convert DAE into a purely algebraic system of equations. The APMonitor then calls nonlinear programming solvers such as Advanced Process OPTimizer (APOPT), Interior Point OPTimizer (IPOPT) or BIM-based Performance OPTimizer (BPOPT) to solve the reduced equations [64].

Th APMonitor has 9 different modes of modelling simulation, three of which are steady-state modes (Steady-state simulation, Model parameter update, Real-time optimization), four are dynamic modes (Dynamic simulation, Moving horizon estimation, Nonlinear control) and the rest can be used either in steady-state or dynamic mode (Sequential dynamic simulation, estimation, or optimization) [64]. In steady-state mode, all the time derivatives are set to zero, while the opposite is true in the dynamic simulation. In this thesis, two modes were used, the steady-state simulation for the steady-state modelling, and the sequential dynamic simulation for the dynamic-state modelling. Values obtained from the steady-state modelling were used to initiate the dynamic simulation. Finally, IPOPT was specified as the solver.

IPOPT uses the interior point method to find the optimal solution of the model. In this method, a feasible region is defined by approximating the constraints defined in the model as boundaries of this region. Search of the optimal solution is then focused in this region through iterative means using Newton's method. The solution is said to be found if the Karush-Kuhn-Tucker conditions, which are basically first derivative tests, are all satisfied [65].

3.1.6 Model verification

To verify the model used in this thesis, the system of Gullberg [58] was considered. The verification involved replicating the temperature oscillations obtained through pressure ramping at different points in time. To make the comparison, the result reported by Gullberg was extracted and plotted with the result obtained from my model. The pressure ramping consisted of decreasing the pressure from an initial value of 150 bar to to 125 bar after 0.5 h, increasing it back to 150 bar after 5 h, and finally decreasing to 115 bar after 10 h. Results show that despite adopting the exact equations used by the author, a different profile was obtained at the first few hours of ramping (Figure 3.3). In my result, the oscillation started at around 1 h, while in the Gullberg's results, the oscillation occurred at a later time, at around 3 h. Nevertheless, after 5 h, a similar profile was observed.

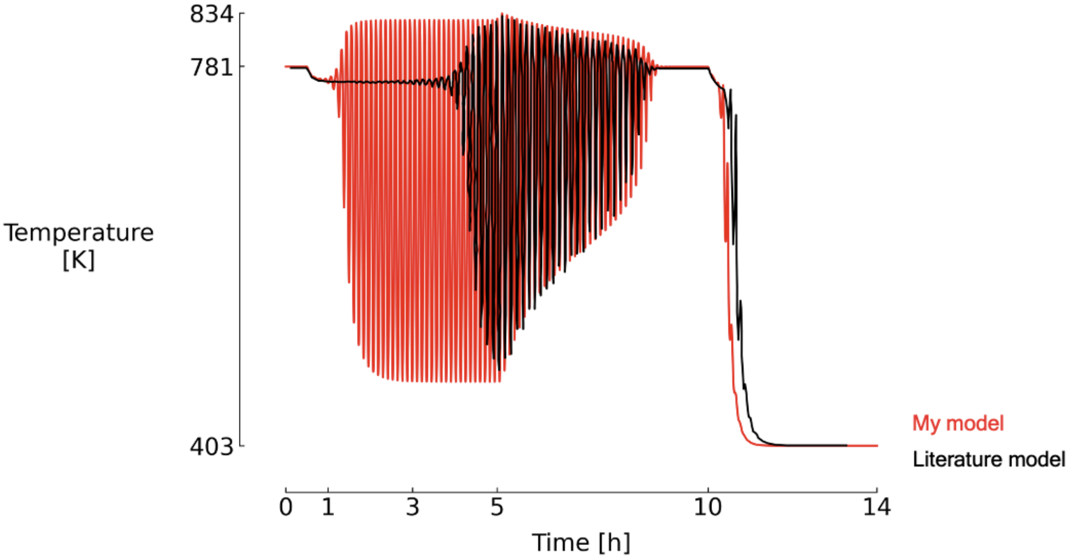

Figure 3.3: Model verification revealed early onset of oscillation obtained in my model (1 h), relative to the results reported by Gullberg [58], where oscillations only become noticeable after 3 h. This difference is believed to be due to the solution found by IDAS being not able to satisfy all Karush-Kuhn-Tucker conditions, which is the basis of IPOPT convergence.

It is important to mention that the parameter values used in my model were the same as in the work of Gullberg. The only difference is that a different framework, called CasADi [66], and IDAS was used in Gullberg's work, while GEKKO with IPOPT was used in this thesis. Experimentation with different volumetric compartments ($nc = 10, 30, 60$) with my model revealed that all oscillations started at the same time (1 h) as reported in Figure 3.3. In comparison, Gullberg reported an early onset (1 h) in oscillations for $nc = 30$. This result suggests that different solutions have been found by the two solvers. Indeed, as previously mentioned, the IPOPT uses the Newton method to find the optimal solution in the feasible region which satisfies all the Karush-Kuhn-Tucker conditions. On the other hand, IDAS uses backward differentiation formulas to solve the dynamic model. Since the IPOPT converges based on how well the conditions are met, it is possible that solutions found by IDAS does not satisfy all the conditions, leading the IPOPT to find another solution and converge with such solution. This would explain why the same starting time is obtained by GEKKO despite the volumetric considered, which is contrary to the case of IDAS.

3.1.7 Reactor volume design

The purpose of calculating the reactor bed volumes at this stage is to ensure that the capacity of the system is at least equal to 50000 kg NH_3/day. This capacity was chosen as it corresponds with Thyssenkrupp's micro-plant, which was specifically developed for power-to-ammonia application [67]. Although the capacity reported by Gullberg [58] is close to the target value (55000 kg NH_3/day), the proposed system consisted only of two reactor beds. Khademi et al. [33] had studied the effect of the number of reactor beds on conversion, energy savings, capital and maintenance cost, and concluded three beds to be the most efficient. As such, efforts were made to convert Gullberg's two-bed system ($V_{\text{total}} = 2\,\text{m}^3$) into a three-bed system.

According to Cheema et al. [36], the optimum reactor design volume can be achieved by maintaining the outlet bed temperatures at 90% of the equilibrium temperature. This is because, an infinite volume is needed to reach equilibrium. By setting such limitation, the maximum possible reaction rate is achieved [36]. The equilibrium temperature was obtained by setting $r_{\text{N}_2} = 0$ in Equation 3.7 and solving the equation in terms of temperature for a chosen range of N_2 conversion (X_{N_2}). The sum of the difference between the outlet bed temperatures ($T_{out,i}$) and 90% of the equilibrium temperature ($T_{0.9EQ}$) were then minimized while the NH_3 production is maximized ($\dot{n}_{\text{NH}_3,net}$), to obtain the maximum possible reaction rate. This was carried out by allowing the inlet bed temperature ($T_{in,i}$) and reactor volumes ($V_{bed,i}$) to vary, as summarized below.

$$\begin{aligned} \text{Minimize} : T_{diff} &= \sum_{i}^{n}(T_{0.9EQ} - T_{out,i}) \\ \text{Maximize} : \dot{n}_{\text{NH}_3,net} &= \dot{n}_{\text{NH}_3,out} - \dot{n}_{\text{NH}_3,in} \\ \text{Constraint} : 0 &\leq X_{\text{N}_2} \leq 0.3, V_{total} = 2m^3 \\ \text{Decision variables} : &\, T_{in,i}, V_{bed,i} \end{aligned}$$

From this, the following volumes for the first, second and third were obtained : $0.561\,\text{m}^3$, $0.708\,\text{m}^3$, and $0.834\,\text{m}^3$.

3.2 Multi-objective Optimization

In this section, the methodology adopted for the multi-objective optimization is detailed. First, the scenario considered for the optimization is described. Then, the optimization problem for the DDO and RDO are explained. The DDO was done by searching for solutions in the design space which were subjected to certain constraints, while the RDO further considers the uncertainties during optimization, as defined in the stochastic space. Lastly, the objective algorithm and uncertainty quantification method will then be explained, where both of these methods are employed in the RDO.

3.2.1 Optimization scenario

In power-to-ammonia technology, renewable energy is used to power the electrolyzer, producing the H_2 needed for ammonia synthesis. The variability of the renewable energy results to changes in the generated electricity, and in turn, causes fluctuations in the H_2 production through time. As the HBS loop was not designed for flexible operation, storage tanks can be incorporated to increase its flexibility [68]. However, the size of the tank needs to be large enough to effectively buffer the fluctuations in H_2 production, with systems powered by wind requiring capacities of 3.5 days of equivalent full load [68], making it expensive. Aside from the cost, H_2 storage is complicated (-254 °C or 350 bar), making it more challenging when dealing with large capacities. Considering that the heart of the HBS loop is the reactor system [20], one way of going around this is to use a small buffer tank and a reactor system designed to be resilient to a certain degree of disturbance in the H_2/N_2 ratio. This resilient system is said to be capable of returning back to normal operating conditions after the disturbance is removed. Therefore, the scenario considered for the optimization involved ramping of the H_2/N_2 stoichiometric ratio for a total duration of 55 minutes. First, the H_2/N_2 ratio was ramped down from 3/1 to 1.31/2.69 [20] after 1 minute steady-state operation. Then, this ratio was maintained for 7 minutes. After 32 minutes, it was then ramped back up to 3/1 (Figure 3.4).

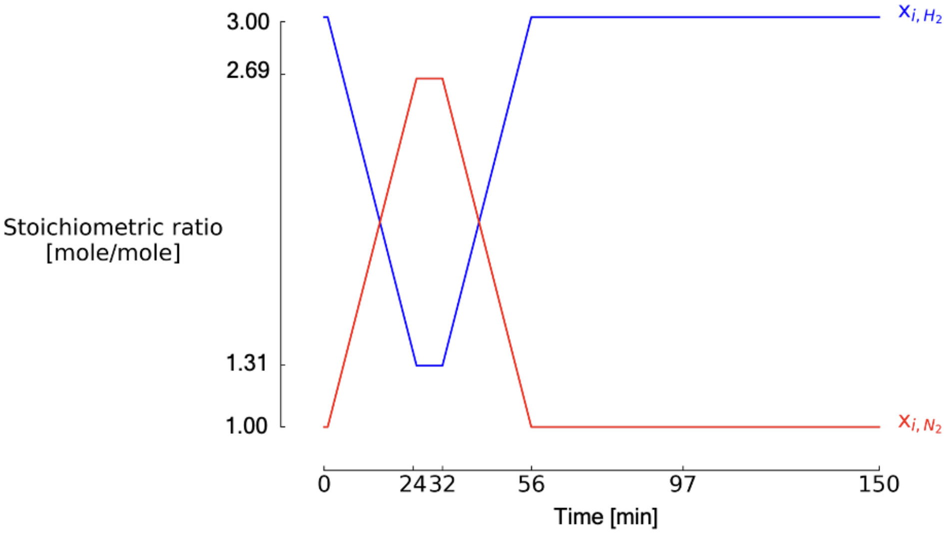

Figure 3.4: The optimization scenario considered in this thesis consisted of ramping the H_2/N_2 stoichiometric ratio from 3/1 to 1.31/2.69 at 1 minutes, for a duration of 24 minutes, maintaining this ratio for 7 minutes, and ramping the ratio back to initial value at 32 minutes, for 24 minutes. Despite ramping being finished at 56 minutes, 150 minutes was considered for the optimization to account for any delays in the temperature recovery.

Both the ramping profile and duration, as well as the 7 minute time interval in-between rampings were based on the work of [56], who studied the scheduling and capacity planning of ammonia production powered by renewable energies. Despite the total ramping being executed for 56 minutes, a 150 minute duration was considered for the optimization to account for any delayed recovery of the system.

3.2.2 Optimization objectives

During periods of low H_2 production due to temporary decrease in wind energy, it can be expected that the reaction rate decreases accordingly, leading to a decrease in the temperature inside the reactor. When the temperature becomes too low for the reaction to be facilitated, the system is said to be extinguished. Thus, it is desired that recovery of the temperature back to normal operation occurs after ramping. In other words, a system exhibiting high temperature resilience is needed. The calculation of the temperature resilience of the system is based on the definition of resilience by Gao et al. [69]. Specifically, the temperature resilience is based on the outlet conditions of the reactor system (outlet of bed 3) and is written as shown

$$R_{\text{temperature}} = \frac{\int_{t_0}^{t_n} T(t)dt}{T(t_0)} \tag{3.21}$$

which is to be maximized. Here $R_{\text{temperature}}$ refers to the temperature resilience of the system for the duration considered (150 minutes), t_0 is the time at which ramping was first initiated (1 minute), and t_n is the final time considered. On the other hand, it is further desired that extraction of the maximum possible NH_3 is made and for this, the net NH_3 output flow rate (kmol/s) is maximized, as shown

$$n_{\text{NH}_3,net} = n_{\text{NH}_3,\text{out}} - n_{\text{NH}_3,\text{in}} \tag{3.22}$$

Therefore a multi-objective optimization was carried out in this thesis, with the goal of maximizing both temperature resilience and net NH_3 output flow rate. As it is desired to determine the effect of cooling system configuration and the reactor volume on the temperature resilience under the scenario described, a total of four deterministic optimization cases were made. For the first objective, two systems of the same reactor bed volumes but different cooling configuration, that is, one is directly quenched, while the other is indirectly quenched, were considered. For the second objective, the reactor volumes of each cooling configurations were optimized in terms of maximum temperature resilience and maximum net NH_3 output flow rate.

Following the deterministic optimization, the cooling system configuration yielding the highest temperature resilience was then robustified against uncertainties. The objective of the robust optimization was to maximize the mean net NH_3 output flow rate, while minimizing its standard deviation under the presence of uncertainties. By focusing on the net NH_3 production during robust design optimization, a resilient design is obtained which produces NH_3 reliably.

3.2.3 Design space

During optimization, the design space is searched for optimal solutions that satisfies the objectives specified. Here, maximization of both the net NH_3 output flow rate and temperature resilience was done by considering the split fraction ratio, area of the heat exchangers, feed pressure and feed molar flow rate as decision variables when investigating the effect of cooling system configurations. The reactor volumes were further included as decision variables when considering the effect of the reactor volume. The main purpose of including the split fraction ratio and area of the heat exchangers as decision variables is to control the inlet temperature of the beds. Due to the deactivation of catalysts at high temperatures [32, 33], constraints [36] were imposed on the inlet temperatures of the beds as shown

$$623\,K \leq T_{\text{bed}} \leq 850\,K \tag{3.23}$$

In choosing the range of values for the decision variables of the first objectives (Table 3.1), the typical operating range of the HBS loop were first identified from the literature, and then imposed in the model. This was the case for the feed pressure where a range of 150 bar to 300 bar [20] was reported. However, for other decision variables such as the feed molar flow rate and area of the heat exchanger, initial results showed that the solution saturated at upper limit value [58, 70]. Therefore, these were adjusted accordingly until saturation was not observed anymore. For the feed molar flow rate, a range of 0.1kmole/s [58] to 2 kmole/s was found to be sufficient, while for the area of the heat exchangers, 1 m^2 to 150 m^2 was chosen. In terms of the split ratio, the range depended on the cooling configuration considered since each configuration had different number of valves (Figure 3.1). The split ratio was defined as the fraction of the feed that goes into the mixer which was controlled using valves. For the indirectly quenched system, since the feed is split only one time, the range was simply taken to be 0 to 1. A different way of assignment was made for the directly quenched system since the feed is split three times. To allow inclusion of a wide range of inlet temperature for beds 2 and 3, it was assumed that up to 90% of the initial feed can be directed to quenching while the remaining 10% was for controlling the inlet temperature of bed 1 (Figure 3.1). This lower split ratio allocation for bed 1 was chosen because of the area of heat exchanger being a decision variable.

Table 3.1: The design space for studying the effect of cooling system configuration on temperature resilience. Range of values were based on literature [20, 58, 70] and adjusted accordingly.

Decision variable	**Units**	**Direct quenching**	**Indirect quenching**
Split ratio quench 1	-	0 - 0.45	0 - 1
Split ratio quench 2	-	0 - 0.45	
Split ratio quench 3	-	0 - 1	
Feed pressure	bar	150 - 300	
Area of heat exchanger	m^2	1 - 150	
Feed molar flow rate	kmol/s	0.1 - 2	

For the second objective, the range of values for the reactor bed volumes were taken as 0.3 m^3 to 10^3 m^3[57]. Since larger reactor volumes were considered in this objective, the feed molar flow rate and area of the heat exchangers were adjusted to 0.1 kmol/s to 10 kmol/s and 1 m^2 to 250 m^2, respectively, while the range of the rest of the variables were adopted from the first objective (Table 3.2).

Table 3.2: The design space for studying the effect of reactor volume on temperature resilience. The inclusion of higher reactor volumes causes the feed molar flow rate and area of the heat exchangers to be adjusted accordingly. Ranges of the remaining variables are from the first objective (Table 3.1).

Decision variable	**Units**	**Direct quenching**	**Indirect quenching**
Split ratio quench 1	-	0 - 0.45	0 - 1
Split ratio quench 2	-	0 - 0.45	
Split ratio quench 3	-	0 - 1	
Feed pressure	bar	150 - 300	
Area of heat exchanger	m^2	1 - 250	
Feed molar flow rate	kmol/s	0.1 - 10	
Volume of bed 1	m^3	0.3 - 10	
Volume of bed 2	m^3	0.3 - 10	
Volume of bed 3	m^3	0.3 - 10	

3.2.4 Stochastic space

The characterization of the uncertainties were based on two things, its distribution and deviation with respect to the mean [71]. There are two types of distribution considered for uncertainties, the Uniform distribution and the Gaussian distribution. The Uniform distribution is typically chosen for operational parameters or when knowledge on the uncertainty is lacking, while the Gaussian distribution is best used for uncertainties associated with the natural randomness. Five parameters were considered uncertain (Table 3.3), two of which are operational and the rest are parametric. In the global sensitivity analysis done by Verleysen et al. [72], it was shown that the HBS loop was highly sensitive to the inlet H_2/N_2 ratio and inlet temperature to the reactor system T_i. In terms of parametric sensitivity, Lassak et al. [73] had shown the contribution of the heat of reaction ΔH_{rxn} to be significant. On the other hand, the heat capacity of the gas $C_{p,gas}$ and catalyst $C_{p,cat}$ were further considered as uncertain. Since the H_2/N_2 ratio is an operational parameter, a Uniform distribution was assumed. On the other hand, the inlet temperature to the reactor system, heat capacity of the gas and solid, and heat of the reaction were taken as Gaussian distributions. Lastly, the mean and standard deviation used in the calculation of the deviation of uncertainties were adopted from the literature [72, 73].

Table 3.3: Summary of the implemented operational and parametric uncertainties into the reactor system. The mean and standard deviation obtained from [72] and [73].

Operational uncertainty	**Distribution**	**Mean**	**Standard Deviation**	**Unit**	**Ref.**
H_2/N_2 ratio	Uniform	2.75	0.14	-	[72]
T_i	Gaussian	673	6.67	K	[72]
Parametric uncertainty					
ΔH_{rxn}	Gaussain	-92.0	2.30	kJ/mol_{N_2}	[73]
$C_{p,gas}$	Gaussian	3500	175	J/kg·K	[73]
$C_{p,cat}$	Gaussian	1100	55	J/kg·K	[73]

3.2.5 Optimization algorithm

When doing multi-objective optimization, it is often the case that no single solution can be designated as best for all the objectives considered. Rather, there exist a set of non-dominated solutions or Pareto solutions which inhibits optimized solutions in the chosen objectives by changing the design variables, forming a Pareto front [74]. Genetic algorithms had been a popular choice for doing multi-objective optimization due to its ability to find the Pareto solutions in one single simulation run, which is not the case for classical optimization methods such as method of objective weighting, method of distance functions and minimum-maximum formulation [74]. Among the genetic algorithms, the Non-dominated Sorting Genetic Algorithm - II (NSGA-II), has shown promise, outperforming other genetic algorithms such as Pareto-archived evolution strategy and strength-Pareto evolultion algorithm in terms of solution diversity and convergence near the actual Pareto solutions [75]. In this study, NSGA-II was adopted as the multi-objective design optimization algorithm.

The concept behind finding the Pareto solutions using NSGA-II can be illustrated in Figure 3.5, where the tth generation is considered. The algorithm starts by generating an offspring population Q_t of the same sample size from the parent population P_t of N samples through cross-over and mutation. Together, P_t and N_t comprise an overall population R_t with $2N$ samples. To identify the parent population for the next iteration P_{t+1}, R_t undergoes two sorting mechanisms, the non-dominated sorting and crowding distance sorting. In the non-dominated sorting, the samples in R_t are ranked according to dominance, where the best non-dominated solution set F_1 is prioritized to be passed on to P_{t+1}. If $F_1 < N$, the second best non-dominated solution set F_2 will be included, and so on until P_{t+1} is completed. To guarantee the same N for P_{t+1}, crowding distance sorting is performed on the last solution set. Basically, for a solutions with the same non-dominance ranking, solutions with larger proximity with other solutions (crowded) will be chosen over solutions in less crowded region to comprise the remaining slots in P_{t+1}. This allows a uniformly spread-out Pareto front to be generated. On the other hand, solutions which were not chosen will be discarded. This P_{t+1} will then be used for the generation of the next off-spring population, continuing to do so until the Pareto solutions are found [75].

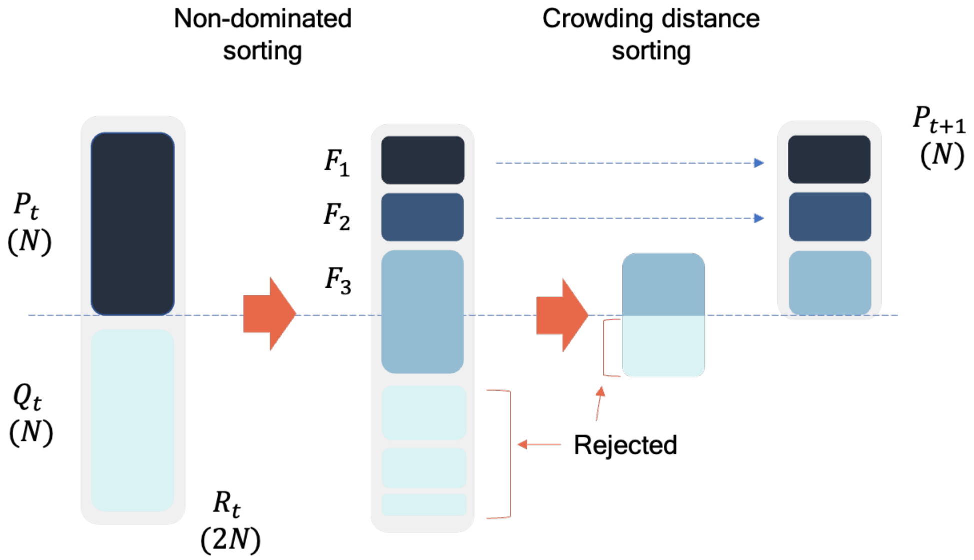

Figure 3.5: The NSGA-II finds the optimal solution by first creating an offspring population Q_t from the parent population P_t through cross-over and mutation. Non-dominated sorting is then performed on the overall population R_t to ensure elitism. When not all of the elements in the population can be accommodated as members of the new parent population P_{t+1}, crowding distance sorting is used. Diagram modified from [75].

The NSGA-II used in this thesis was obtained through the Robust design optimization of renewable Hydrogen and dErIved energy cArrier systems (RHEIA) framework. A population size of 24 was used for all cases studied with a computational budget of 2000.

3.2.6 Uncertainty quantification method

In practice, the input parameters of a system are not characterized by a constant, single value. Rather, the values are uncertain which can be expressed in terms of the mean, the relative deviation and the distribution. To propagate the uncertainty of input parameters to the system model, the Polynomial Chaos Expansion (PCE) was used. The PCE was developed by Sudret et al. [76] as an alternative method to the robust yet inefficient Monte Carlo simulation. The popularity of the PCE is largely due to its emphasis on calculation efficiency, which makes the statistics of computationally demanding models faster to retrieve [76]. This high efficiency of the PCE can be attributed to the use of a surrogate model $\mathcal{M}^{PCE}$, which is an approximation of the model $\mathcal{M}$. This $\mathcal{M}^{PCE}$ is expressed as series of orthogonal polynomials ψ and its corresponding coefficients u, as shown below

$$\mathcal{M}^{PCE}(X) = \sum_{\alpha \in \mathcal{A}} u_\alpha \psi_\alpha(X) \approx \mathcal{M}(X) \tag{3.24}$$

where α are the multi-indices and $\mathcal{A}$ is the considered set of multi-indices. When $\mathcal{A}$ is equal to infinity, the surrogate model is the real model. Truncation is typically done, and is given as

$$|\mathcal{A}^{M,p}| = \frac{(M+p)!}{M!p!} \tag{3.25}$$

where p corresponds to the polynomial order and M is the number of uncertainties or stochastic dimension. Cross validation is then done to assess how well the $\mathcal{M}^{PCE}$ had modelled $\mathcal{M}$. To this end, the leave-one-out (LOO) cross validation can be used [76]. The validation involves generation of multiple PCE from a set of sample with one point being left out $x^{(i)}$. In other words, a PCE model $\mathcal{M}^{PCE}$ is generated from the remaining $n-1$ samples, and the error $\widehat{Err}_{LOO}$ with respect to the original model $\mathcal{M}$ is calculated as shown

$$\widehat{Err}_{LOO} = \frac{1}{n}\sum_{i=1}^{n}(\mathcal{M}(x^{(i)}) - \mathcal{M}^{PCE}(x^{(i)}))^2 \tag{3.26}$$

If the LOO error is less than a certain specified value, it is supposed that $\mathcal{M}^{PCE}$ can accurately represent the $\mathcal{M}$. We can analytically derive the mean μ and the standard deviation σ, as follows

$$\mu = u_0 \tag{3.27}$$

$$\sigma^2 = \sum_{i=1}^{P} u_i^2 \tag{3.28}$$

Aside from the statistical moments, the contribution of each stochastic parameter on the output of interest can be quantified through Sobol' indices. The total Sobol' indices $S_i^{T,PC}$ quantifies the total impact, including all mutual interactions.

$$S_i^{T,PC} = \frac{\sum_{\alpha}^{A_i^T} u_{\alpha}^2}{\sigma^2} \qquad A_i^T = \alpha \in A | \alpha_i > 0 \tag{3.29}$$

As with the NSGA-II, the PCE was obtained through RHEIA. An LOO ≤ 0.001 was set as the limit of $\mathcal{M}^{PCE}$ accurately approximating the $\mathcal{M}$. Identification of p involved examining the LOO error starting from order 1 until 5. At $p > 5$, the quantification is considered computationally expensive and the $\mathcal{M}^{PCE}$ was declared as not being able to accurately approximate the model. In this case, quantification of uncertainty involves identification of the worst-case scenarios, which corresponds to the lowest and highest values of each stochastic parameters.

Chapter 4

Results and Discussion

The discussion in this chapter is divided into two main sections, the deterministic design optimization (DDO) and the robust design optimization (RDO). The purpose of doing a DDO is to identify designs with the most temperature resilience (most R) and the most net NH_3 output flow rate (most NH_3). These extreme designs are then used as basis for identifying the effect of the cooling system configuration and the reactor volume on the temperature resilience. The influence of uncertainties on the deterministic designs will then be discussed by subjecting the extreme deterministic designs to worst-case scenarios. Finally, the RDO of the most resilient system will be detailed.

4.1 Deterministic design optimization

The DDO was performed on the direct and the indirectly quenched system, first with the previously calculated volume and secondly, where each system's volume is optimized. A population of 24 samples was selected for each DDO, and using NSGA-II as the optimization algorithm, converged to set of solutions which maximizes the net output NH_3 flow rate, as well as the temperature resilience in varying degrees. In what follows, the effect of cooling system is first discussed, followed by the effect of reactor volume on temperature resilience.

Objective 1: Effect of cooling system

Directly quenched system

The DDO of the directly quenched system yielded a set of non-dominated solutions which reveal a design trade-off between the net NH_3 output flow rate and temperature resilience (Figure 4.1). Although a good compromise between the two objectives exist (highlighted in yellow, Figure 4.1), the most R design was chosen for further analysis as this design resulted to the lowest temperature drop inside the reactor, which is important for catalyst integrity. To illustrate, the temperature drop obtained with the compromised resilience design (150 K) is 2.27 times higher compared to the most R design (66 K).

The most NH_3 design resulted to a net output of 0.0741 kmol/s, which is 2.07 times larger than the most R design (0.0358 kmol/s). In turn, the higher net output of the most NH_3 design is compensated by its resilience (0.941), which is 1.05 times lower than the most R design (0.941) (Table 4.1).

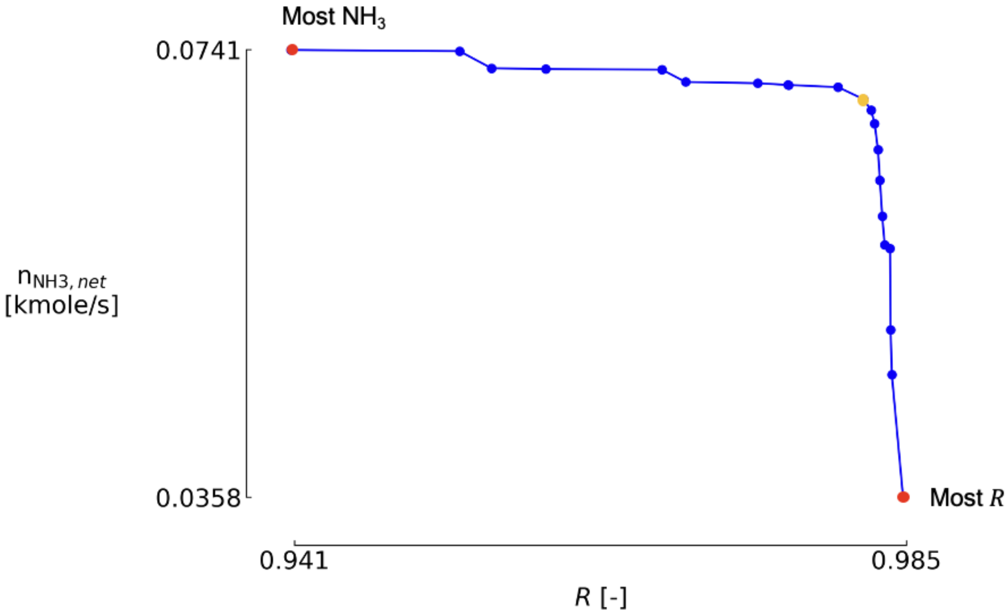

Figure 4.1: The DDO of the directly quenched system resulted to a design trade-off when maximizing for the net NH_3 output flow rate ($n_{NH_3,net}$) and temperature resilience (R). The Pareto solution highlighted in yellow refers to the compromised design.

To operate in the most NH_3 design, a feed pressure of 267 bar and a feed molar flow rate of 0.530 kmol/s are required. The split ratio of the quench stream and area of the heat exchanger needs to be configured (Table 4.1) such that the inlet temperatures of bed 1, 2, and 3 are 627 K, 661 K, and 802 K, respectively. On the other hand, operation at the most R design requires a pressure of 184 bar, a feed molar flow rate of 0.400 kmol/s, and inlet bed temperatures of 626 K, 779 K and 806 K for beds 1, 2 and 3, respectively. When comparing the operating conditions between the two extreme designs, the most NH_3 design operates at a pressure and feed molar flow rate that is 1.45 times and 1.33 times higher than the most R design, respectively. However, the inlet bed temperatures of the most NH_3 design are generally lower than the most R design. This need for higher pressure, higher feed molar flow rate and lower inlet temperatures by the most NH_3 design is expected as higher pressure and higher reactant concentration drives the equilibrium to more NH_3 production, while lower temperature favors equilibrium for exothermic reactions, in accordance to the Le Chatelier's principle.

Table 4.1: Set of decision variables, resulting inlet bed temperatures and objective values of the extreme designs of the directly quenched system.

Decision variable	**Units**	**Case**	
		Most NH_3	**Most R**
Split ratio quench 1, u_1	-	0.00945	0.00945
Split ratio quench 2, u_2	-	0.377	0.0256
Split ratio quench 3, u_3	-	0.132	0.034
Feed pressure, P_f	bar	267	184
Area of heat exchanger, A_{HX}	m^2	32.9	67.2
Feed molar flow rate, n_f	kmol/s	0.530	0.400
Inlet bed temperatures			
Inlet temperature of bed 1, $T_{i,1}$	K	627	626
Inlet temperature of bed 2, $T_{i,2}$	K	661	779
Inlet temperature of bed 3, $T_{i,3}$	K	802	806
Objective values			
Net NH_3 output flow rate, n_{NH_3}	kmol NH_3/s	0.0741	0.0358
Temperature resilience, R	-	0.941	0.985

Examination of the temperature profile with time at the outlet of bed 3 (Figure 4.2) shows that, for the most NH_3 design, the ramp-down in the H_2/N_2 ratio during the first 25 minutes resulted to a decrease in temperature, followed by the onset of temperature oscillations at the start of ramp-up (32 minutes). These oscillations continued even after ramping (56 minutes), and recovery to normal operation is observed at 97 minutes. The oscillation profile obtained for the most NH_3 design is characterized by amplitudes which increase and then decrease after reaching a maximum. The lowest temperature (422 K) is obtained during ramp-up, at 45 minutes. On the other hand, for the most R design, a similar temperature response is initially observed, except that smaller amplitudes were obtained which slowly continue to dampen after 150 minutes. Unlike the most NH_3 design, the largest temperature drop for the most R design (66 K) is obtained prior to the onset of oscillations, that is, at the lowest H_2/N_2 ratio (32 minutes).

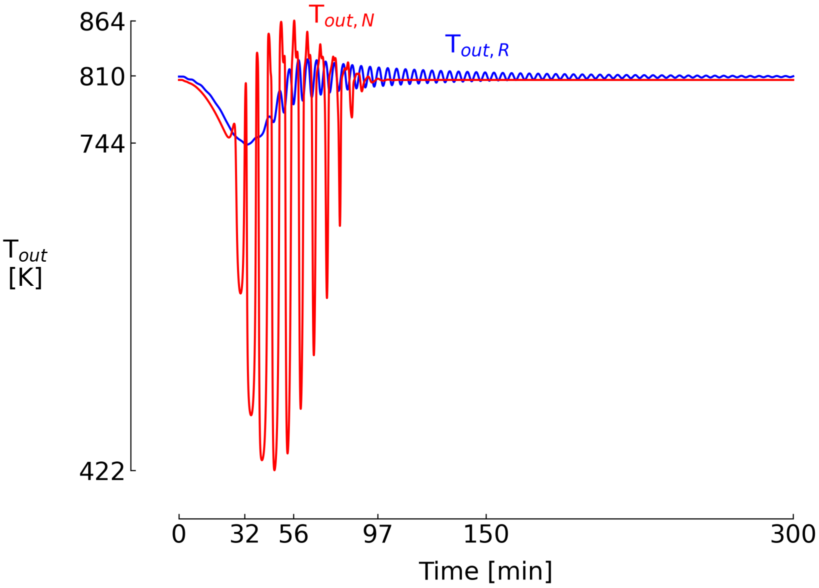

Figure 4.2: Temperature profile of the directly quenched system with time during ramping for the most NH_3 ($T_{out,N}$) and most R ($T_{out,R}$) designs. Ramp-down of H_2/N_2 from 3/1 to 1.31/2.69 is carried out in the first 25 minutes, followed by no disturbance for 7 minutes, and then ramp-up back to 3/1 for another 24 minutes.

To explain the difference in the oscillation profile between the most NH_3 design and the most R design, it is important to first discuss the concept of stability in a dynamic industrial reactor. For this, we refer to the bifurcation study done by Mancusi et al [77] for a directly quenched ammonia reactor. In this study, the temperature was obtained by varying the pressure to yield the solution diagram. The value reported for the temperature in the solution diagram depended on whether the dynamic system reached steady-state temperatures, or if limit cycle was observed. If the former case is attained, the temperature value was taken to be the steady-state outlet temperature value of the reactor, while, if the later case is observed, the maximum outlet temperature value attained during the oscillations was used. The solution diagram revealed an S-shape profile between the temperature and pressure, which represents three branches - the stable high conversion branch, the stable low conversion branch, and the unstable stationary branch (Figure A.1).

The stable high conversion branch corresponds to sets of temperature and pressure values that would result to a stable dynamic system with high reactant conversions. Likewise, a system operating at the stable low conversion branch will converge to the indicated temperature and pressure values as its steady-state values, but with lower conversions. On the other hand, operation at the unstable stationary state results to an unstable limit cycle behavior which eventually extinguishes to the stable low conversion value. It is important to mention here that transition from one state to another is possible by either manipulating the temperature or pressure, as in the case of Mancusi's study. The author further stated that around the lower limit of the stable high conversion branch, a shift from steady-state solution to periodic solution is possible, as defined by a critical point called the Hopf bifurcation. Furthermore, the stability of the periodic solution depends on which region or more accurately speaking, fold bifurcation, the system is in. The fold bifurcation immediate to this Hopf bifurcation (F_3) is characterized by unstable periodic solutions, while the next fold bifurcation, located further from the Hopf bifurcation (F_2) is characterized by stable periodic solutions (Figure A.1). As such, a system can have stable oscillations characterized by amplitudes of constant size, or unstable oscillations which can either return to the upper steady-state solutions or proceed to the unstable stationary branch, eventually reaching the stable low conversion branch, corresponding to extinction.

Therefore, in Figure 4.2, the reason why the most NH_3 design exhibited an early oscillation which recovers after ramping is that, the system is operating around the fold bifurcation close to the Hopf bifurcation in the stable high conversion branch (F_3). On the contrary, the most R design is operating around the fold bifurcation corresponding to stable oscillations (F_2). Indeed, by operating close to the Hopf bifurcation (F_3), which, as mentioned before, is a critical point of transition between stable to periodic solutions or vice versa, the system was able to recover to steady-state temperature value after the oscillations. The manifestation of the instability as oscillations instead of extinction can be explained through the inverse-response behavior experienced during sudden changes at the inlet conditions [57]. In this case, as the H_2 concentration is decreased, the reaction rate around the inlet of the bed decreases, and thus the temperature around the inlet as well. This causes the temperature around the outlet of the bed to appear relatively higher when compared to the temperature around the inlet. Therefore, as the temperature propagates through the bed, it will first exhibit a decreasing profile and then slowly change into an increasing profile as it approaches the outlet of the bed. As such, a wave-like profile is obtained which leads to oscillations.

On the other hand, to explain the larger amplitudes obtained for the most NH_3 design relative to the most R design, we refer to the H_2 concentration profile of both designs with time (Figure 4.3). Initially, the outlet H_2 concentration for the most NH_3 design is $2.35\,\mathrm{kmol/m^3}$, which reduces to $0.88\,\mathrm{kmol/m^3}$ after the full ramp-down. As the ratio is ramped up, oscillations are observed, where recovery to steady-state value is attained after 97 minutes. For the most R design, the initial outlet H_2 concentration is 1.71 kmol/m^3, and drops to 0.67 kmol/m^3 after the ramp-down. In comparison, the largest drop in H_2 concentration for the most NH_3 design is 1.47 kmol/m^3, which is 1.41 times larger than the most R design (1.04 kmol/s). This larger drop in concentration is expected as the most NH_3 design requires a feed molar flow rate which is 1.33 times higher than the most R design. By experiencing a larger drop in concentration, the changes in the outlet temperature is also larger for the most NH_3 design compared to the most R design. As such, when conditions corresponding to the fold bifurcations are reached, the corresponding amplitudes of the oscillations will also be higher.

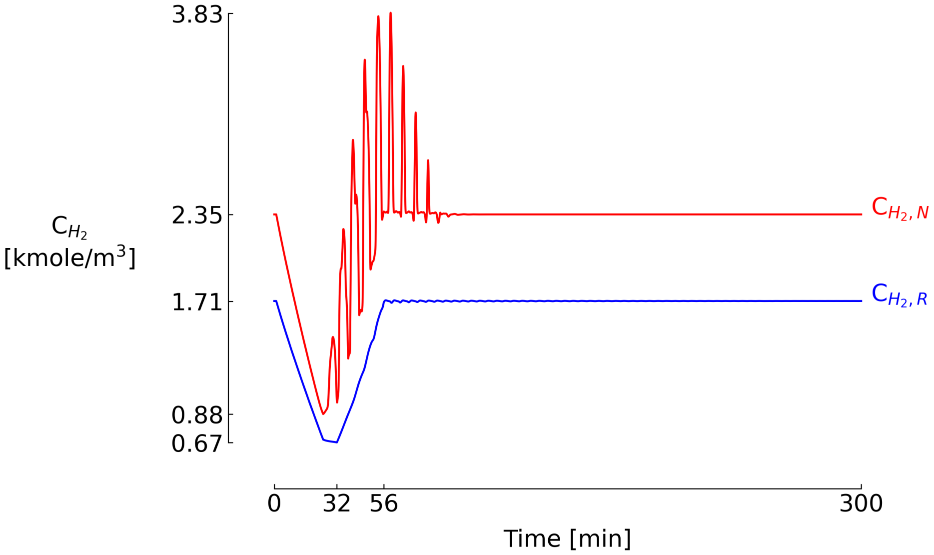

Figure 4.3: H_2 concentration profile with time for the most NH_3 ($C_{H2,N}$) and most R ($C_{H2,R}$) design of directly quenched system. Oscillations in the $C_{H2,N}$ observed for the most NH_3 design is a feedback from the oscillations observed in the temperature. Ramp-down of H_2/N_2 from 3/1 to 1.31/2.69 is carried out in the first 25 minutes, followed by no disturbance for 7 minutes, and then ramp-up back to 3/1 for another 24 minutes.

The influence of the operating conditions and the H_2 concentration on the outlet temperature between the extreme designs can be seen in Figure 4.4. During ramp-down, negative values of the reaction rate (outlet) for the most NH_3 design were obtained, followed by oscillation to positive values at the start of ramp-up, eventually including negative values during oscillations. The same can be said about the most R design except that smaller oscillations were attained, with a mean reaction rate of around the equilibrium value ($r_{H_2} = 0$). As previously mentioned, the most NH_3 design operates such that the equilibrium is shifted towards the production of NH_3 (higher pressure and feed molar flow rate, but lower inlet temperatures). Therefore, as the H_2 concentration was increased from ramp-up, the larger amounts of H_2 introduced into the system resulted to a dramatic increase in its reaction rate. On the other hand, the smaller feed molar flow rate specified for the most R design is not enough to induce a large increase in the reaction rate at the same order as observed in the most NH_3 design. Because of this, despite operating at lower inlet bed temperatures, the most NH_3 design exhibits larger changes in the temperature compared to the most R design. As a consequence, the smaller drop observed for the most R design allows for easier recovery to normal temperature operation after ramping, resulting to higher resilience than the most NH_3 design.

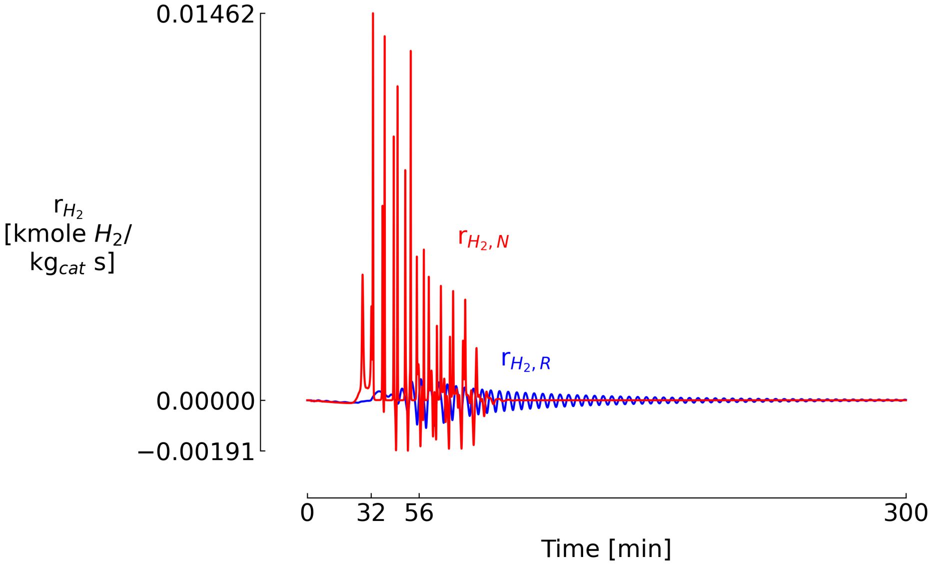

Figure 4.4: Reaction rate profile of directly quenched system showing the larger variations in the reaction rate for the most NH_3 design ($r_{H2,N}$) relative to the most R design ($r_{H2,R}$) with time.

Indirectly quenched system

The DDO of the indirectly quenched system converged to 24 generally non-dominated solutions, revealing design trade-offs when maximizing for the net NH_3 output flow rate and temperature resilience (Figure 4.5). The most NH_3 design resulted to a net output rate of 0.0510 kmol NH_3/s, which is slightly higher than the most R design (0.0506 kmol NH_3/s). In turn, the resilience of the most

NH_3 design is 0.976, which is slightly lower than the resilience of the most R design (0.979). This small trade-off between the extreme designs was expected since a limitation was imposed on the search space to only include designs which exhibited recovery to normal operation after ramping. Although this constraint was also imposed for directly quenched system, this small trade-off highlights the operational inflexibility of the indirectly quenched system relative to the directly quenched system. As explained next, a delicate balance need to be respected to operate autothermally. Therefore, despite such small trade-off, it is still important to proceed with the separate discussion of the extreme designs to better understand resilient operation for indirectly quenched system, and to have a basis of comparison for the extreme designs of the directly quenched system.

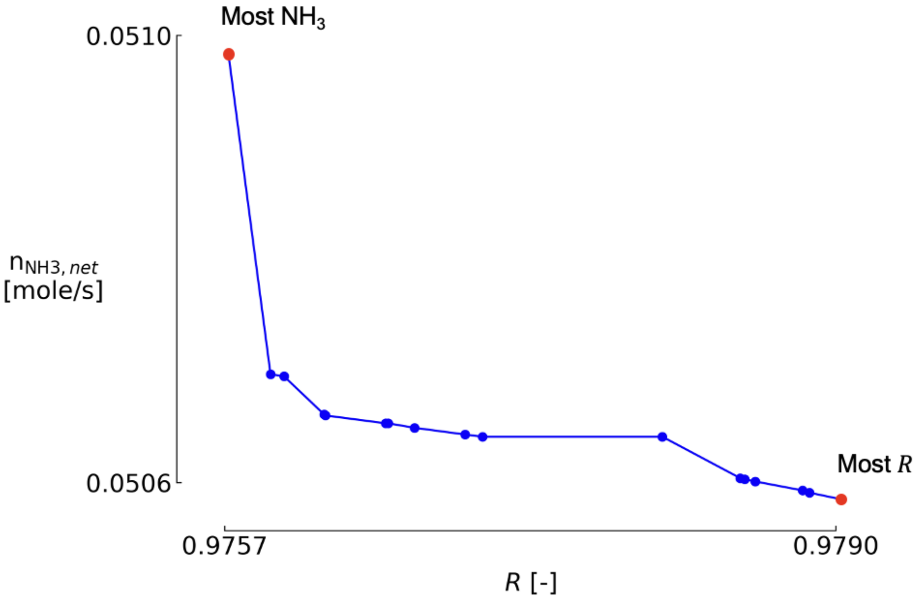

Figure 4.5: The DDO of the indirectly quenched system resulted to a small design trade-off when maximizing for the net NH_3 output flow rate ($n_{NH_3,net}$) and temperature resilience (R).

To operate at the most NH_3 design, a feed pressure of 238 bar and a feed molar flow rate of 0.382 kmol/s are required. The split ratio of the quench stream and the heat exchanger area needs to be configured (Table 4.2) such that the inlet temperatures of bed 1, 2, and 3 are 696 K, 697 K, and 802 K, respectively. The same feed pressure and feed molar flow rate are required to operate at the most R design, however, higher inlet temperatures for bed 1, 2, and 3 are needed. This need for the same feed pressure and feed molar flow rate between the two extreme designs of the indirectly quenched system can be explained by first discussing how autothermal operation is achieved for this system. As mentioned in the previous chapter, the cold feed enters at the first reactor bed, where it then exits as a hot stream. This hot exit stream then proceeds to the heat exchanger where cooling takes place through indirect contact with the cold incoming feed. Therefore, achieving autothermal operation depends on the balance between the all inlet and outlet temperatures, which in turn, are interconnected (Figure 4.6). It is believed that by imposing a constant reactor volume, differentiation between the most extreme designs was limited to the inlet bed temperatures.

Table 4.2: Set of decision variables, resulting inlet bed temperature and objective values of the extreme designs for the indirectly quenched system.

Decision variable	**Units**	**Case**	
		Most NH_3	**Most R**
Split ratio, u	-	0.785	0.906
Feed pressure, P_f	bar	238	238
Area of heat exchanger 1, $A_{HX,1}$	m^2	91.8	122
Area of heat exchanger 2, $A_{HX,2}$	m^2	33.3	28.8
Area of heat exchanger 3, $A_{HX,3}$	m^2	18.8	18.8
Feed molar flow rate, n_f	kmol/s	0.382	0.382
Inlet bed temperatures			
Inlet temperature of bed 1, $T_{i,1}$	K	696	696
Inlet temperature of bed 2, $T_{i,2}$	K	697	705
Inlet temperature of bed 3, $T_{i,3}$	K	624	626
Objective values			
Net NH_3 output flow rate, $n_{NH_3,net}$	kmol NH_3/s	0.0510	0.0506
Temperature resilience, R	-	0.976	0.979

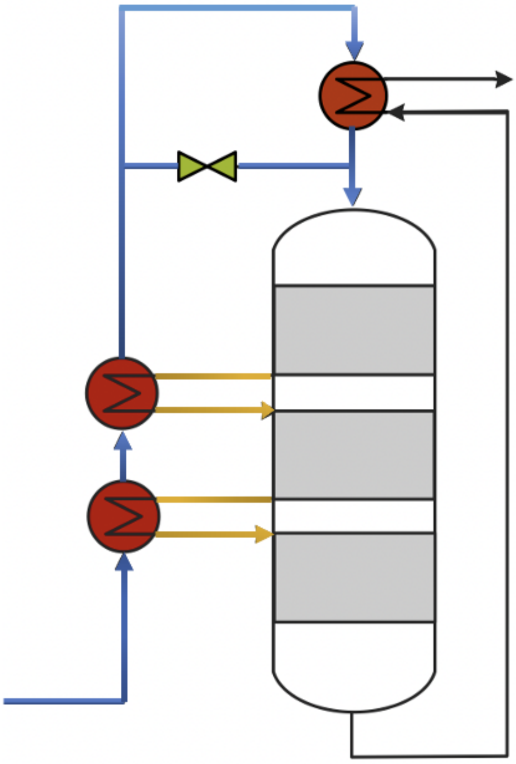

Figure 4.6: The cold feed stream (blue line) enters the reactor bed and exits as hot exit stream (yellow line), where it then enters the heat exchanger. In the heat exchanger, the hot exit stream comes in indirect contact with the incoming cold feed stream to achieve the desired inlet temperature of the next bed.

Inspection of the outlet temperature of bed 3 with time shows that for both extreme designs, recovery to normal operating temperatures were successful after ramping at 55 minutes (Figure 4.7). For the most NH_3 design, initial ramp-down resulted to a momentary peak in the outlet temperature (9 minutes), followed by a decrease up until the early stage of ramp-up (36 minutes). This corresponding dip in the temperature resulted to a maximum temperature drop of 107 K, for the most NH_3 design. The same can be said for the most R design, except that the maximum temperature drop is 94 K. This similarity in outlet temperature profile between the two extreme designs is expected since both designs operate at the same feed pressure and feed molar flow rate, with the only exception of inlet bed temperatures. As the most R design operates at a slightly higher inlet temperature, its outlet temperature is correspondingly higher than the most NH_3 design.

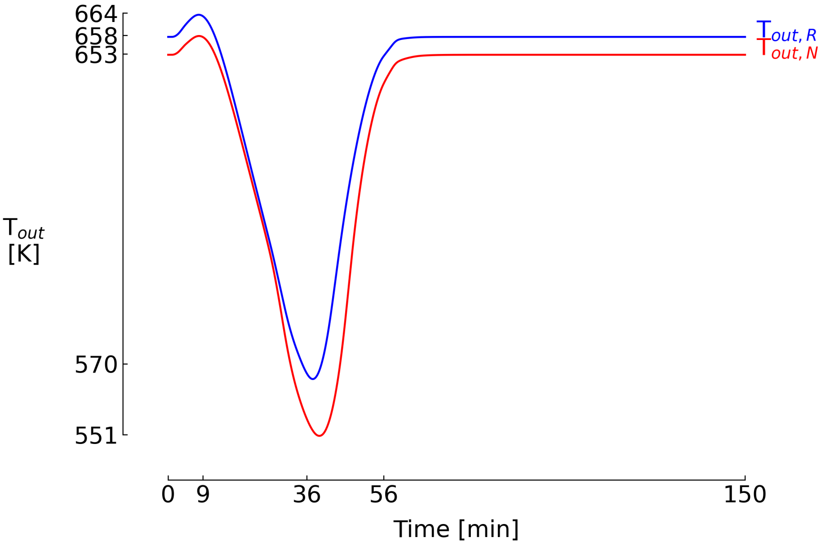

Figure 4.7: Temperature profile of the indirectly quenched system with time during ramping for the most NH_3 ($T_{out,N}$) and most R ($T_{out,R}$) designs. Ramp-down of H_2/N_2 from 3.0 to 1.5 is carried out in the first 24 minutes, followed by no disturbance for 7 minutes, and then ramp-up back to 3.0 for another 24 minutes.

To understand why temperature recovery was attained for both extreme designs of the indirectly quenched system without oscillations, it is important to first discuss the difference in its operating conditions with respect to the directly quenched system (Table 4.1). The indirectly quenched system operates at a feed molar flow rate is at least 0.018 kmole/s lower than the directly quenched system. In terms of the inlet bed temperatures, the values range from 623 to 705 K, for the indirectly quenched system, while a range of 626 K to 806 K is observed for the directly quenched system. This operation at lower feed molar flow rate and lower inlet bed temperatures which is limited to a small range is believed to be the reason why recovery without oscillations was possible for both extreme designs of the indirectly quenched system. That is, at lower feed molar flow rate, the experienced drop in the amount of H_2 during ramp-down will not be as dramatic as when the feed molar flow rate is high (Figure 4.3). Furthermore, by operating at a lower temperature, a slower reaction rate can be realized, making the temperature changes not as dramatic (Figure 4.7). Because of this, the system stays at the stable high conversion branch during ramping, and recovers more easily afterward.

Nevertheless, a higher resilience was obtained for the most R designs of the directly quenched system (0.985) compared to the indirectly quenched system (0.979). This is because with directly quenched system, the feed is split into fractions which enter the reactor beds in smaller amounts. As such, a smaller amount of H_2 is reacted at each bed compared to the indirectly quenched system, where all of the feed is reacted at the same time. Therefore, the changes in the reaction rate is not as dramatic in the direct quenching compared to when more feed is reacted, as in indirect quenching (Figure 4.8). Ultimately, this results to minimal changes in temperature and thus higher resilience.

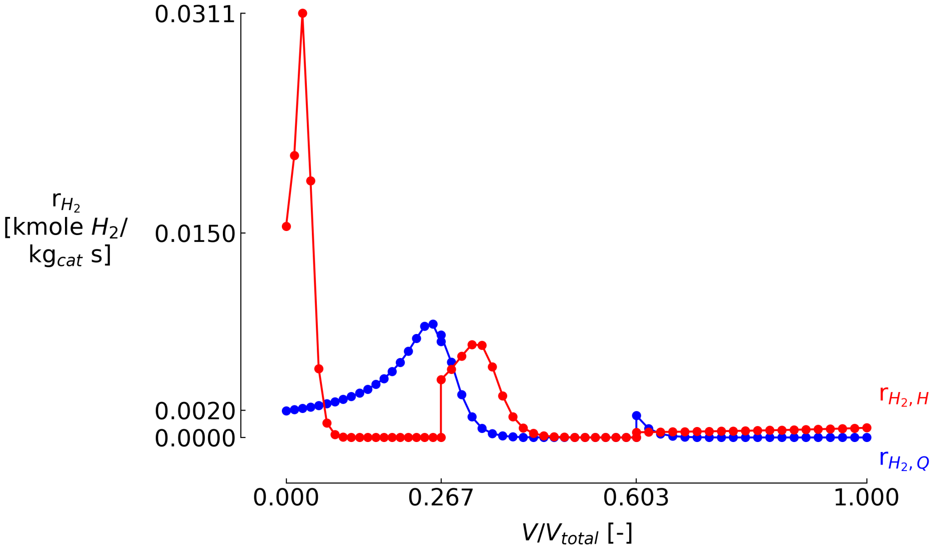

Figure 4.8: Reaction rate profile of the indirectly quenched ($r_{H2,H}$) and directly quenched system ($r_{H2,Q}$) with respect to bed volume fraction, showing the larger variations in the reaction rate for the former compared to the later.

Therefore, when considering the best design between the two configurations for power-to-ammonia applications, we need to consider not just the resilience of the system but also the temperature profile inside the reactor. As previously shown, the directly quenched system resulted to the highest resilience between the two configurations. However, oscillations are observed in its temperature profile for both extreme designs (Figure 4.2). Although these oscillations can be prevented by choosing a compromised design (Figure 4.1), the temperature drop obtained in such design (150 K) is 1.40 times higher than the largest temperature drop (107 K) obtained for the indirectly quenched system (most NH_3 design). When considering the most R design of both configurations, the directly quenched system has a resilience of 0.985, which is slightly higher (0.006) than the indirectly quenched system (0.979). In turn, the difference in terms of the largest temperature drop between the direct (66 K) and indirectly quenched system (94 K) is 28 K. Furthermore, because of the lower residence time in the directly quenched system compared to the indirectly quenched system [20], a higher output is obtained for the indirectly quenched system for a lower feed molar flow rate. Despite the limited range of operation (feed pressure and feed molar flow rate) for the indirectly quenched system (Table 4.2), it is still perceived as the best design for power-to-ammonia applications due to its high resilience without the manifestation of oscillations, and high net NH_3 output flow rate. Moreover, the feed pressure and feed molar flow rate can be kept constant by manipulating the argon concentration in the feed [20].

Objective 2: Effect of reactor volume

Directly quenched system

The DDO of directly quenched system converged to 24 solutions, revealing a design trade-off between the two conflicting objectives (Figure 4.9). The most NH_3 design resulted to a net NH_3 output flow rate of 0.362 kmol/s, which is 19 times larger compared to the most R design (0.0191 kmol/s). In turn, the resilience of the most NH_3 design is slightly smaller (0.983) compared to the most R design (0.987).

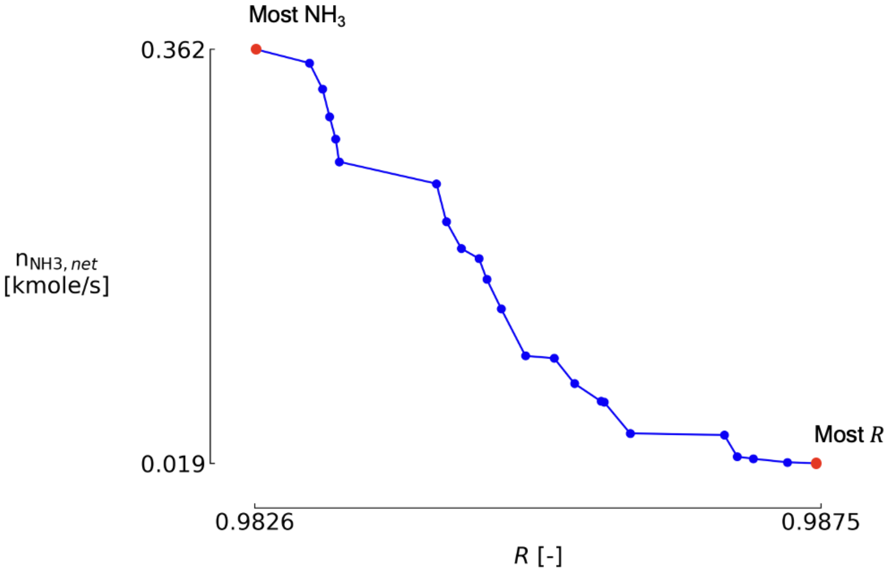

Figure 4.9: The DDO of the directly quenched system with optimized volume resulted to a design trade-off when maximizing for the net NH_3 output flow rate ($n_{NH_3,net}$) and temperature resilience (R).

Operation at the most NH_3 design requires a feed pressure of 296 bar and a feed molar flow rate of 2.84 kmol/s, while the inlet temperature of beds 1, 2 and 3 need to be at 626 K, 775 K and 777 K, respectively (Table 4.3). In comparison, the feed pressure and feed molar flow rate for the most R design are 1.13 and 15.5 times lower than the most NH_3 design (263 bar and 0.183 kmol/s). Also, slightly higher inlet bed temperatures are needed for the most R design, which are 654 K, 812 K and 816 K for beds 1, 2 and 3, respectively. This need for lower feed pressure and feed molar flow rate, as well as higher inlet bed temperatures agrees with the previous result of the directly quenched system. In terms of the optimized bed volumes, the most NH_3 design requires a volume of 9.78 m^3, 2.28 m^3, and 4.73 m^3 for beds 1, 2 and 3, respectively. Similar results are obtained for the most R design, with volumes for bed 1 and 3 being slightly lower (9.73 m^3 and 4.65 m^3) than the most NH_3 design.

Table 4.3: Set of decision variables, resulting inlet bed temperatures and objective values of the extreme designs of the directly quenched system, yielding its optimized volume design.

Decision variable	**Units**	**Case**	
		Most NH_3	**Most R**
Split ratio quench 1, u_1	-	0.117	0.0500
Split ratio quench 2, u_2	-	0.126	0.0677
Split ratio quench 3, u_3	-	0.038	0.038
Feed pressure, P_f	bar	296	263
Area of heat exchanger, A_{HX}	m^2	191	222
Feed molar flow rate, n_f	kmol/s	2.84	0.183
Volume of bed 1, V_1	m^3	9.78	9.73
Volume of bed 2, V_2	m^3	2.28	2.28
Volume of bed 3, V_3	m^3	4.73	4.65
Inlet bed temperatures			
Inlet temperature of bed 1, $T_{i,1}$	K	626	654
Inlet temperature of bed 2, $T_{i,2}$	K	775	812
Inlet temperature of bed 3, $T_{i,3}$	K	777	816
Objective values			
Net NH_3 output flow rate, $n_{NH_3,net}$	kmol NH_3/s	0.362	0.0191
Temperature resilience, R	-	0.983	0.988

Investigation of the outlet temperature profile with time for both extreme designs (Figure 4.10) show that recovery is attained in both designs. For the most NH_3 design, the temperature decreases with ramp-down, exhibiting a minimum prior to ramp-up (32 minutes), where it then makes a recovery shortly after the full ramping (56 minutes). This minimum corresponded to the largest temperature drop (82 K) relative to the initial outlet temperature value. For the most R design, the temperature follows a similar profile, but shifted to the right, with the minimum temperature exhibited after the full ramping of the system (68 minutes). This delayed response has the largest temperature drop of 41 K, which is 2 times smaller than the most NH_3 design.

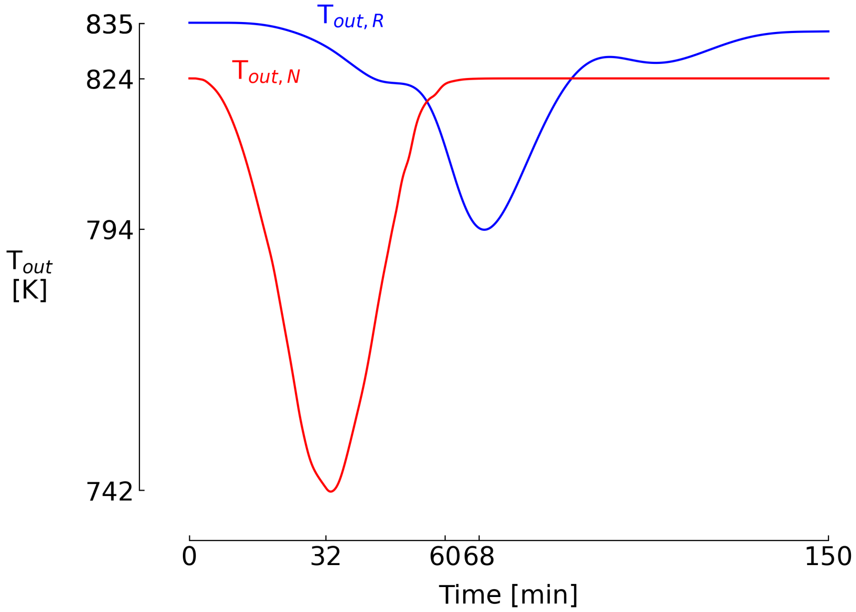

Figure 4.10: Temperature profile of the directly quenched system with optimized volume as a function of time, for the most NH_3 ($T_{out,N}$) and most R ($T_{out,R}$) designs. Ramp-down of H_2/N_2 from 3/1 to 1.31/2.69 is carried out in the first 25 minutes, followed by no disturbance for 7 minutes, and then ramp-up back to 3/1 for another 24 minutes.

It is interesting to point out that, despite specifying the range for each reactor volume to be 0.3 m^3 to 10 m^3, and 0.1 kmole/s to 10 kmole/s for the feed molar flow rate, the NSGA-II selected volumes which are atleast 2.73 times larger than the volumes used in the previous objective (0.561 m^3, 0.708 m^3, and 0.834 m^3), while the corresponding flow rate here was chosen to be 4.30 times higher for the most NH_3 design, but 2.19 times lower when comparing the most R design of the same system from the previous objective. The tendency for larger volume and feed molar flow rate for the most NH_3 design is expected as higher these mean higher NH_3 production capacity, while for the most R design, the combination of lower feed molar flow rate and higher reactor volume allows for the immediate consumption of reactants. This is clearly seen in Figure Figure 4.11, which shows the reaction rate of the most R design for the optimized ($r_{H_2,OV}$) and the non-optimized ($r_{H_2,NOV}$) volume as a function of reactor bed volume fraction, as an example. For the optimized volume, the low molar flow rate resulted to a low H_2 concentration in the bed, causing the reaction rate to decrease with the bed volume fraction and reach equilibrium values near the entrance of the bed. In contrast, for the non-optimized volume, because of the combination of larger flow rate and smaller reactor design, the amount of H_2 that can be consumed per kg catalyst is relatively higher. Because of this, more H_2 can be consumed leading to generation of more heat and temperature to rise. With this increase in temperature, the reaction rate exponentially increases (according to Arrhenius law) until it decreases again as the H_2 are used. In the absence of these fluctuations in the reaction rate, the temperature drop inside the bed will not be as dramatic, thereby increasing the chances for recovery after ramping.

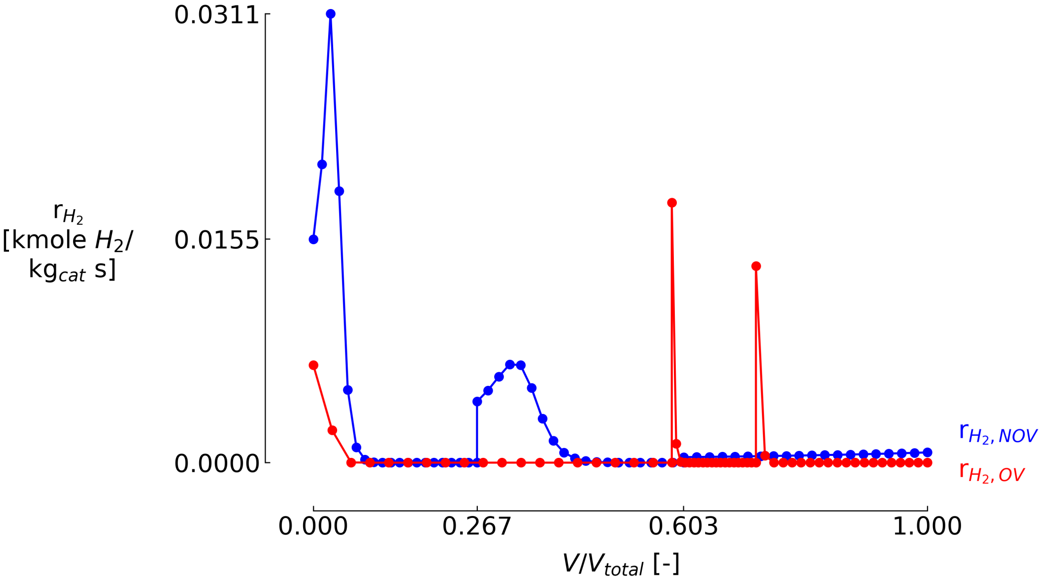

Figure 4.11: The low reaction rate of the most R with optimized volume design ($r_{H_2,OV}$) allowed temperature drops to be not as large compared to if the reaction rate was higher, as observed in the non-optimized volume design ($r_{H_2,NOV}$).

Indeed, when going to larger reactor volumes as obtained in the optimization here, the feed molar flow rate shows an inversely proportional relationship with resilience (Figure 4.12), while the relationship between reactor volume and resilience is not so straightforward (Figure 4.13).

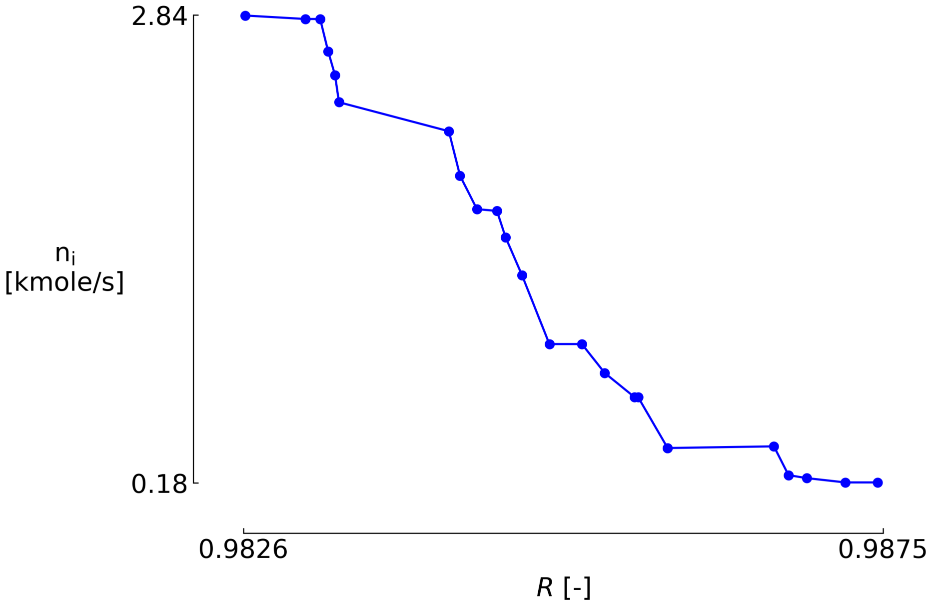

Figure 4.12: Optimization of the reactor volume of directly quenched system show an inversely proportional relationship between feed molar flow rate and resilience.

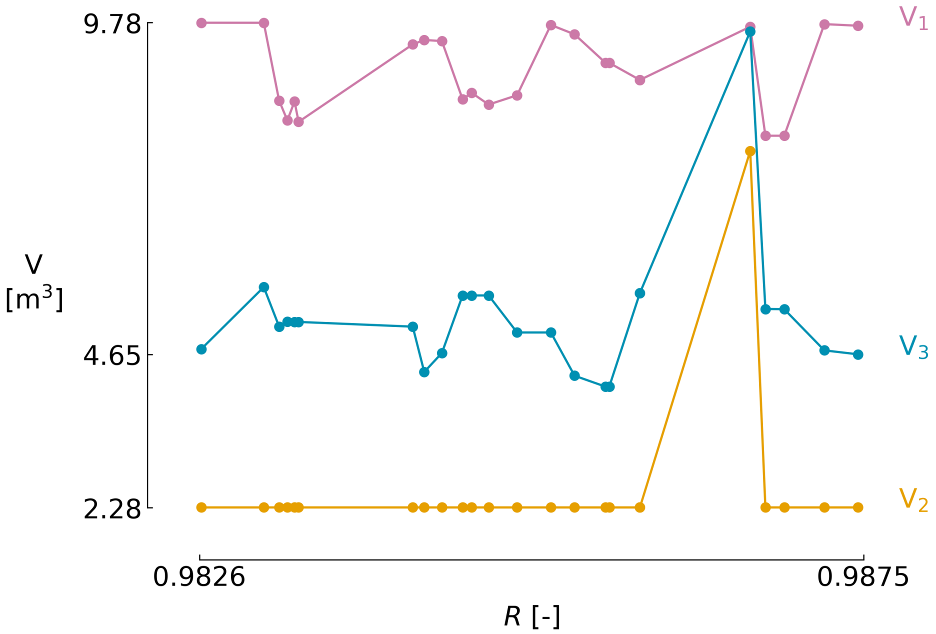

Figure 4.13: Optimization of the reactor volume of directly quenched system shows that resilience to not depend on the reactor volume.

Indirectly quenched system

On the other hand, when optimizing the reactor bed volumes of the indirectly quenched system, 24 generally non-dominated solutions were obtained, which also reveals a design trade-off when maximizing the net NH_3 output flow rate and temperature resilience (Figure 4.14). The most NH_3 design has a net output flow rate of 0.390 kmol/s which is 1.30 times larger than the most R design (0.301 kmol/s). This resulted to a decrease in resilience to 0.960 which is 1.03 times smaller than the most R design (0.985).

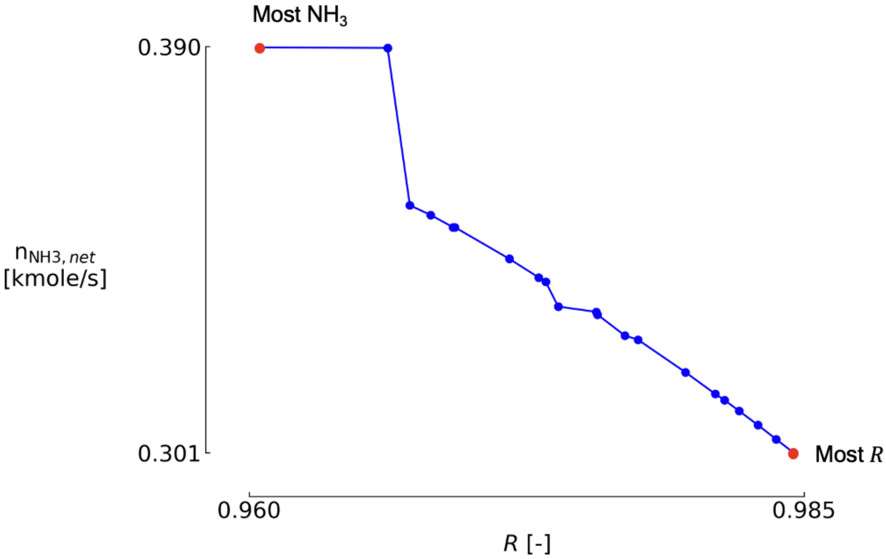

Figure 4.14: The DDO of the indirectly quenched system with optimized volume resulted to a design trade-off when maximizing for the net NH_3 output flow rate ($n_{NH_3,net}$) and temperature resilience (R).

To operate at the most NH_3 design, a feed pressure and feed molar flow rate of 300 bar and 2.26 kmol/s are needed, with inlet bed temperatures being 737 K, 709 K, and 649 K, for beds 1, 2 and 3, respectively. The most R design requires the same feed pressure and feed molar flow rate, but with slightly lower temperatures (694 K, 697 K and 640 K). The operation at the same feed conditions agrees with the result previously obtained for its non-optimized volume. However, in the case of non-optimized volume, the inlet bed temperatures for the most R design was slightly higher than the most NH_3 design. This difference can be interpreted by first mentioning the optimized volumes for both extreme designs. For the most NH_3 design, 3.22 m^3, 4.48 m^3 and 6.66 m^3 are required for beds 1, 2, and 3, respectively, while for the most R design, the same volumes are needed for beds

1 and 2, but a much smaller volume (0.36 m^3) is needed for bed 3. Unlike in the non-optimized volume case where the volumes of both extreme designs are the same, here, by allowing the inlet bed temperature and volume to be small for bed 3, the corresponding outlet temperature drop can be decreased. Indeed, a smaller volume means smaller amount of catalyst, and low inlet bed temperature means a low starting point for the reaction, the amount of heat generated from the reaction is also smaller, resulting to less intense dips in the temperature. As seen in Figure 4.15, the largest temperature drop for the most NH_3 design is 177 K, while the drop is 2.49 times smaller for the most R design (71 K).

Table 4.4: Set of decision variables, resulting inlet bed temperatures and objective values of the extreme designs of the indirectly quenched system, yielding its optimized volume design.

Decision variable	**Units**	**Case**	
		Most NH_3	**Most R**
Split ratio, u	-	0.632	0.632
Feed pressure, P_f	bar	300	300
Area of heat exchanger 1, $A_{HX,1}$	m^2	64.1	64.1
Area of heat exchanger 2, $A_{HX,2}$	m^2	210	210
Area of heat exchanger 3, $A_{HX,3}$	m^2	96.8	96.8
Feed molar flow rate, n_f	kmol/s	2.26	2.26
Volume of bed 1, V_1	m^3	3.22	3.22
Volume of bed 2, V_2	m^3	4.48	4.48
Volume of bed 3, V_3	m^3	6.66	0.36
Inlet bed temperatures			
Inlet temperature of bed 1, $T_{i,1}$	K	737	694
Inlet temperature of bed 2, $T_{i,2}$	K	709	697
Inlet temperature of bed 3, $T_{i,3}$	K	649	640
Objective values			
Net NH_3 output flow rate, $n_{NH_3,net}$	kmol NH_3/s	0.390	0.301
Temperature resilience, R	-	0.960	0.985

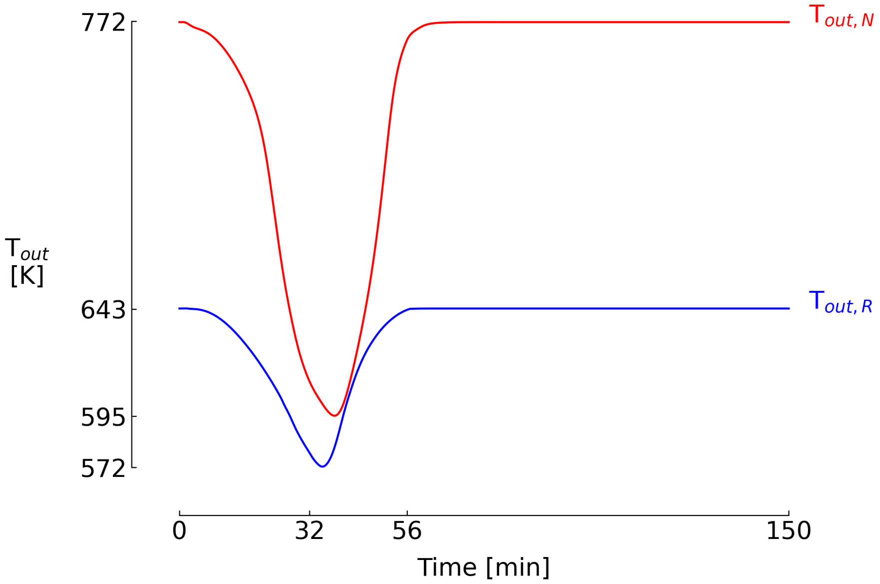

Figure 4.15: The larger drop in temperature observed for the most NH_3 design ($T_{out,N}$) of the indirectly quenched system with optimized volume is due to the larger volume specified for the last bed. The same reasoning applies for the most R design ($T_{out,R}$), where its temperature drop is 2.49 times smaller than the most NH_3 design.

Examination of the evolution of reactor volume with resilience for indirectly quenched system with optimized volume show that the resilience is dependent only on the last reactor volume, bed 3 (Figure 4.16). For beds 1 and 2, a constant volume is obtained for all resilience values. This implies that for indirectly quenched system, higher resilience can be attained if a smaller volume at the last reactor is implemented.

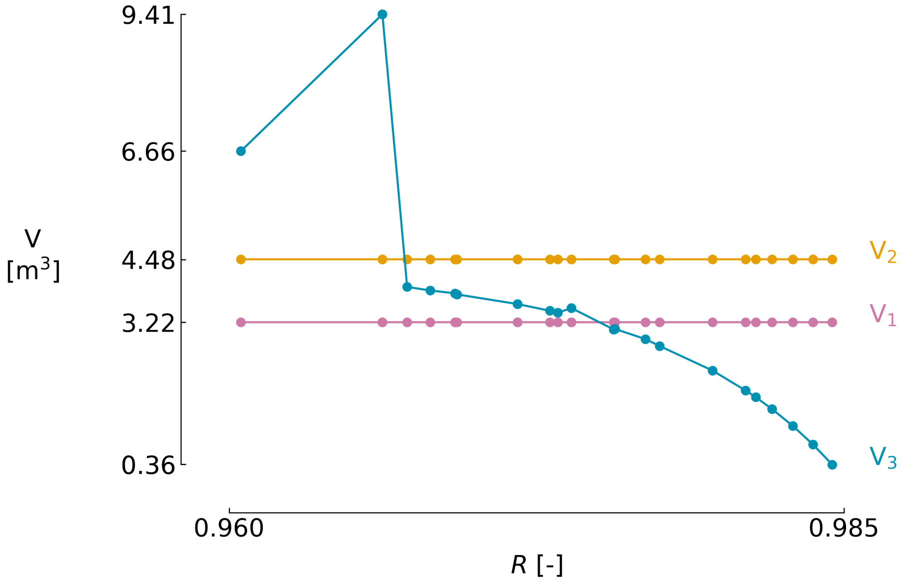

Figure 4.16: Optimization of the reactor volume of indirectly quenched system show resilience increasing with the last reactor volume (V_3).

For both systems, the higher reactor volumes chosen by NSGA-II relative to the previous objective, led to higher temperature resilience for both extreme designs of the directly quenched system. For the indirectly quenched system, an increase in resilience was observed for the most R design but a decrease was seen for the most NH_3 design. Despite an increase in resilience obtained at higher volumes, the temperature resilience of the directly quenched system did not show dependence on the reactor volume (Figure 4.13), however, decreasing the feed molar flow rates resulted to increasing resilience (Figure 4.12). In contrast, an inverse relationship between the last reactor bed and temperature resilience was observed for the indirectly quenched system. Furthermore, no oscillations were seen for all the optimized volume design unlike the previous objective (directly quenched system). Therefore, it is perceived that under the scenario of fluctuating H_2 amount in the feed, operation at higher reactor volume with a smaller flow rate is best (high resilience) for the directly quenched system, while for the indirectly quenched system, opting for a smaller volume at the last bed with higher feed molar flow rate is recommended.

4.2 Effect of uncertainty on deterministic designs

The effect of uncertainties on the deterministic designs was studied by subjecting the extreme designs to worst-case scenarios, defined as the lowest and highest values of the uncertainties. In what follows, the temperature profile of extreme designs are examined under the presence of uncertainties, starting with the directly quenched system, and then indirectly quenched system. For each system, the non-optimized volume design is analyzed first, followed by the optimized volume design.

System 1: Directly quenched system

Figure 4.17 shows that operation of the directly quenched system with non-optimized volume at the lowest values of uncertain parameters resulted to temperature extinction for both extreme designs. The same initial and final outlet temperatures were obtained for both designs, with the most R design achieving extinction at a later time (80 minutes) compared to the most NH_3 design (35 minutes). This corresponded to a decrease in resilience from 0.941 in the deterministic operation to 0.568 in this case for the most NH_3 design, and from 0.985 to 0.602 for the most R design.

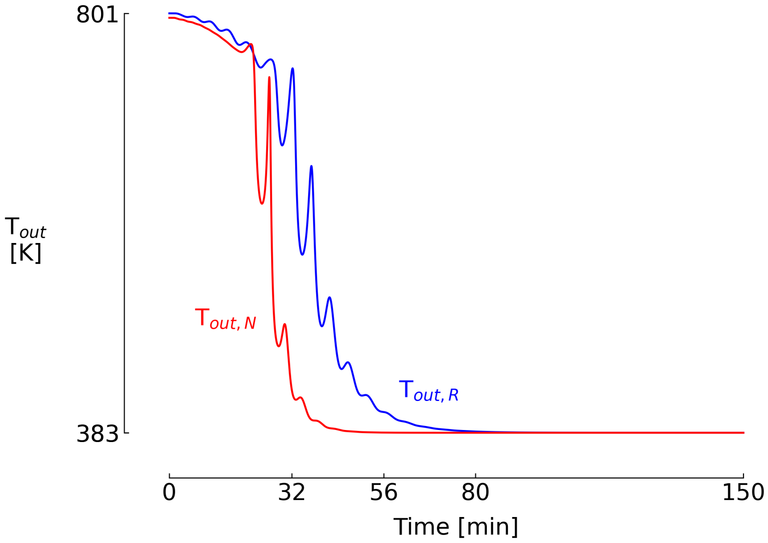

Figure 4.17: Subjecting the directly quenched system with non-optimized volume to the lowest values of uncertainties resulted to reactor extinction for both extreme designs, with the most R design becoming extinct 45 minutes later than the most NH_3 design. The resilience decreased by 0.373 for the most NH_3 design, and by 0.383 for the most R design with respect the resilience obtained from deterministic operation.

The extinction for both designs are expected, since the lowest values of feed temperature, H_2/N_2 ratio, and heat of reaction, among others, were considered. Because the temperature inside the reactor is influenced by the amount of heat generated from the reaction, a lower ratio means that the amount H_2 that can be reacted to generate the heat is also lower. By further taking the lowest value for the heat of reaction and feed temperature, the resulting temperature of the system becomes low enough that extinction is achieved.

On the other hand, the temperature profile of the directly quenched system with optimized volume shows that successful recovery was made when considering the lowest values (-3σ) of the uncertain parameters (Figure 4.18). Nevertheless, a lower initial outlet temperature was obtained here compared to deterministic operation due to operation at lower inlet temperature, H_2/N_2, and heat of reaction values. For the most NH_3 design, the initial outlet temperature was decreased from 824 K to 815 K, while for the most R design, a decrease from 835 K to 826 K is observed. Correspondingly, the resilience dropped from 0.983 to 0.982 for the most NH_3 design, and from 0.988 to 0.987 for the most R design.

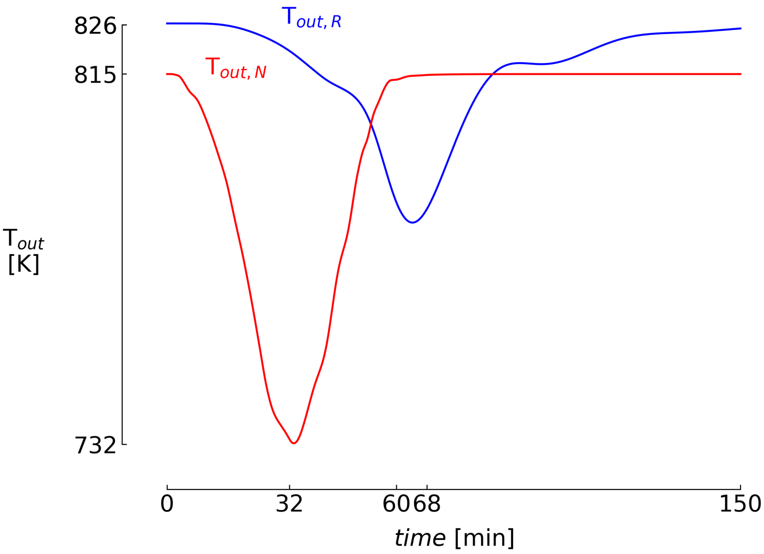

Figure 4.18: Subjecting the directly quenched system with optimized volume to the lowest values of uncertainties resulted to a decrease in the initial outlet temperature with respect to the deterministic operation for both extreme designs. As a result, the resilience decreased by 0.001 for both extreme designs.

The recovery attained by the directly quenched system with optimized volume can be attributed to its larger volume and larger feed molar flow rate compared to the system with non-optimized volume. At these designs, the amount of H_2 consumption is higher, leading to generation of more heat from the reaction. Therefore, despite considering the lowest values for the feed temperature, H_2/N_2 ratio, and heat of reaction, recovery was possible as the temperature was somewhat maintained from the heat generated.

When operating at the highest values of the uncertain parameters, the most R design of the non-optimized volume of directly quenched system showed an increase in the initial outlet temperature, from 810 K in the deterministic operation to 817 K in this case, while recovery to normal operation is attained at 70 minutes which is 17 minutes earlier compared to the recovery from deterministic operation. This corresponded to no change in resilience with respect to deterministic operation. On the other hand, the most NH_3 design showed a decrease in the initial outlet temperature, from 744 K in the deterministic operation to 720 K in this case, and attained a new, higher steady-state temperature value of 817 K at 70 minutes. This jump can be understood by considering that the initial ramping caused the system to be unstable, manifesting the oscillations in temperature, and when ramp-up was done, this supplied the necessary amount of reactants needed by the system to become stable again, at a higher outlet temperature (+ 97 K). Because of this jump, the reported resilience for the most NH_3 design in this case is greater than 1.

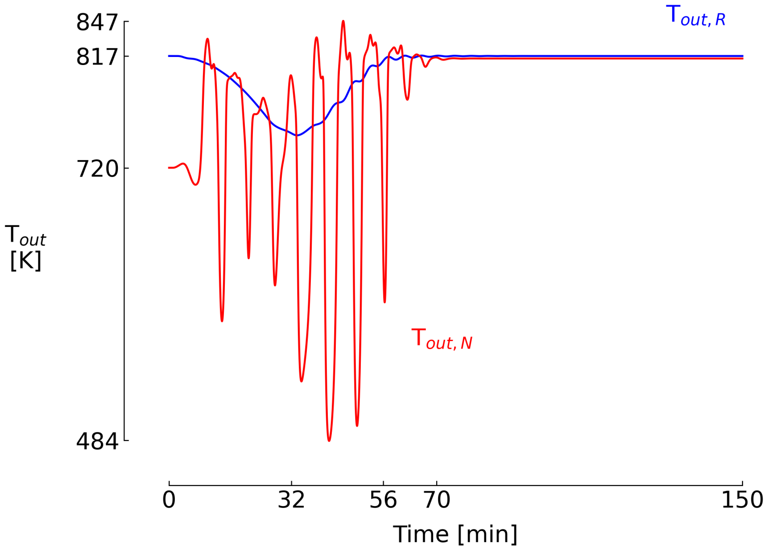

Figure 4.19: Subjecting the directly quenched system with non-optimized volume to the highest values of uncertainties resulted to an increase in the initial outlet temperature with respect to the deterministic operation for the most R design (+ 7 K), but a decrease in the said temperature for the most NH_3 design (- 24 K). The resilience for the most R design is the same as in deterministic operation, while the resilience of the most NH_3 exceeded 1.

A similar situation can be observed for the case of directly quenched system with optimized volume. A higher initial outlet temperature of 844 K for the most R was obtained here compared to the deterministic operation (835 K). However, a further delay in the temperature response from ramping is observed, with the largest dip attained at 75 minutes instead of 68 minutes as in the deterministic case. The resilience here is reported to be the same as in deterministic operation. A larger jump in the outlet temperature (178 K) is observed for the most NH_3 design with the optimized volume relative to the non-optimized volume (97 K) after ramping. This can be attributed to the fact that the feed molar flow rate of the most NH_3 design with the optimized volume is 5.36 times larger than its corresponding non-optimized volume design.

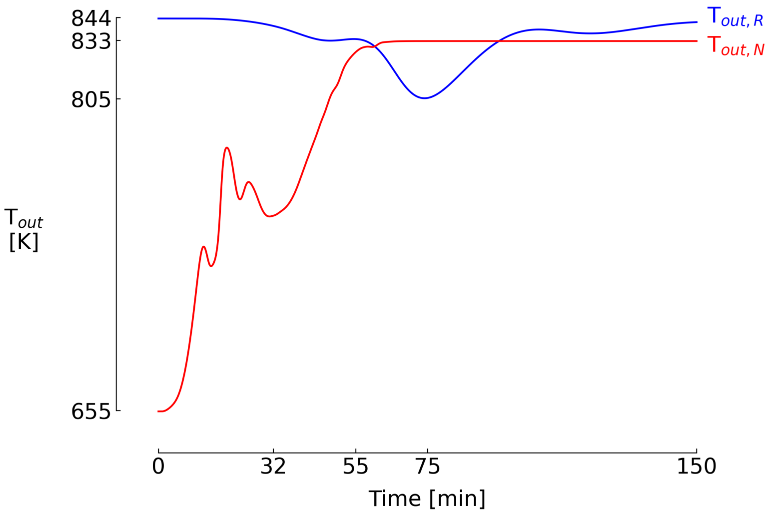

Figure 4.20: Subjecting the directly quenched system with optimized volume to the highest values of uncertainties resulted to an increase in the initial outlet temperature with respect to the deterministic operation for the most R design (+ 9 K), but a decrease in the said temperature for the most NH_3 design (- 169 K). The resilience for the most R design is the same as in deterministic operation, while the resilience of the most NH_3 exceeded 1.

Therefore, under the presence of uncertainties, the use of the optimized volume (larger volume) for the directly quenched system is recommended for better recovery performance. At the low-end values of the uncertain parameters, the optimized volume did not result to reactor extinction, while extinction is observed for the case of non-optimized volume. Although the optimized volume resulted to a shift to higher steady-state temperature values, it is assumed that such case is better compared to reactor extinction, as the later would require special start-up procedures [57], and hence increase in maintenance time.

System 2: Indirectly quenched system

Operation of the indirectly quenched system with non-optimized volume using the lowest value of the uncertain parameters resulted to a reduction in the initial outlet temperature, from 772 K in the deterministic operation to 623 K for the most NH_3 design, and from 643 K to 625 K for the most R design. The temperature profile for both extreme designs are very similar, following the same response with ramping. The ramp-down from these lower initial outlet temperature resulted to a decrease in temperature, followed by a small resistance in temperature due to initiation of ramp-up (32 minutes). The temperature then continues to decrease with extinction (383 K) attained for both extreme designs after the full ramping (55 minutes). As discussed previously, the jump from the stable high conversion branch located at higher temperatures, to the stable low conversion branch can be made through changes in the temperature of the system. Hence, the decrease in temperature brought by ramp-down supported this drop from 625 K to 383 K. The resilience reported for both extreme designs are 0.696, which is lower by 0.28 with respect to deterministic operation for both designs.

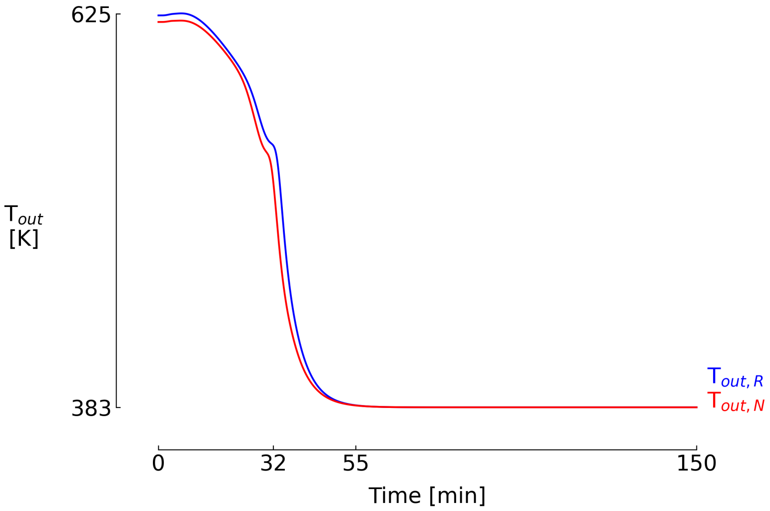

Figure 4.21: Subjecting the indirectly quenched system with non-optimized volume to the lowest values of uncertainties resulted to an decrease in the initial outlet temperature with respect to the deterministic operation for both designs. Consequently, the resilience decreased by 0.28 for both designs.

When examining the effect of operating at the lowest values of the uncertain parameters for the optimized volume of indirectly quenched reactor, no solution was found by GEKKO. This could be due to not finding solutions that satisfies the KKT constraints within the defined feasible region.

On the other hand, examining the effect of the highest values of the uncertain parameters showed that a similar temperature profile is obtained for both extreme designs of indirectly quenched system with non-optimized volume. The same observation was also made for the case of operating at the lowest values of the uncertain parameters were studied (Figure 4.21). For the most NH_3 design, the initial outlet temperature was decreased from 772 K at deterministic operation to 717 K, while its temperature is at the minimum (598 K) at the start of ramp-up (32 minutes, Figure 4.22). For the most R design however, the initial outlet temperature increased from 643 K in the deterministic case to 718 K, in this case (Figure 4.22). A slightly higher minimum temperature of 604 K was obtained for the most R design which was also attained at early ramp-up stage. Despite operating at the highest uncertainty values, a decrease of 0.00422 for the most NH_3 design, and 0.00590 for the most R design was observed in the resilience. This is in contrast to the findings for the directly quenched system, where operation at the highest values either result in the preservation of the resilience or a slight increase with respect to deterministic operation. Nevertheless, the recovery made here is to be expected since higher values of feed temperature, H_2/N_2 and heat of reaction support higher values of outlet temperatures during ramp-down, making recovery more feasible.

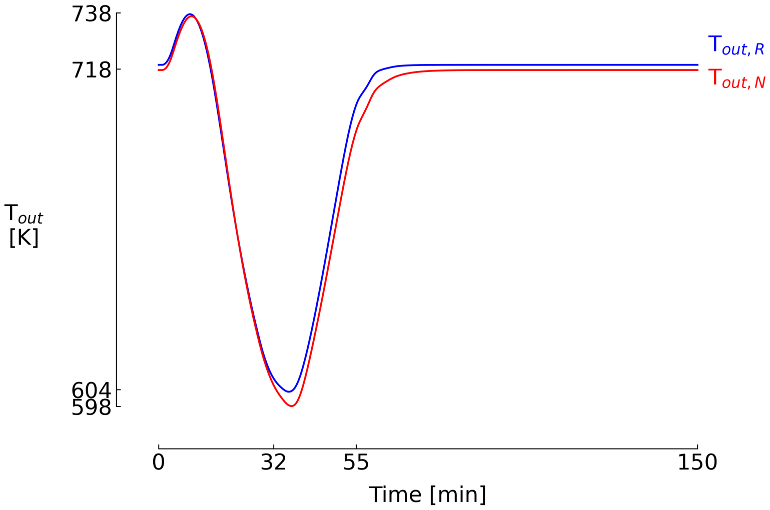

Figure 4.22: Subjecting the indirectly quenched system with non-optimized volume to the highest values of uncertainties resulted to an increase in the initial outlet temperature with respect to the deterministic operation for the most R design (+ 75 K), but a decrease in the said temperature for the most NH_3 design (- 55 K). The corresponded to a decrease of 0.00422 for the most NH_3 design, and 0.00590 for the most R design in terms of the resilience, relative to deterministic operation.

For the optimized volume of the indirectly quenched system, a temporary dip followed by settling to a new, higher steady-state temperature values are observed in its temperature profile, when operating at the highest values of the uncertain parameters. Again, the settling to higher steady-state values is due to the design parameters supporting higher outlet temperatures through larger reactor volumes and higher feed molar flow rate. Because a higher steady-state value is obtained, the resilience are both greater than 1.

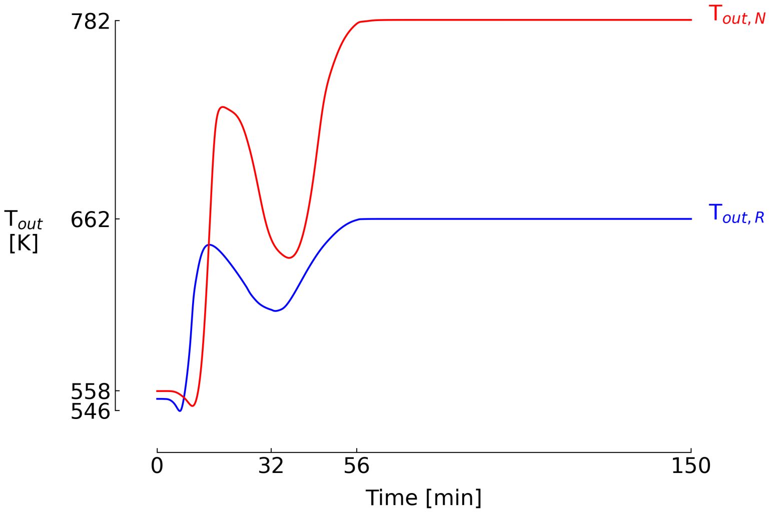

Figure 4.23: Subjecting the indirectly quenched system with optimized volume to the highest values of uncertainties resulted to higher steady-state temperature values, leading to resilience values greater than 1 in both extreme designs.

When operating at non-deterministic parameter values, a similar temperature profile was obtained for both extreme designs of the indirectly quenched system with non-optimized volume. Therefore, either most extreme designs is perceived as best for operation with uncertainties. On the other hand, the optimized design needs to be re-done for recommendations to be made.

4.3 Robust design optimization

As seen in the previous section, subjecting the deterministic designs to the worst-case values of the uncertain parameters can result to reactor extinction or re-settling to a higher steady-state temperature value. The former case is undesirable since the system needs to be re-started to resume operation and therefore losses in terms of NH_3 production are incurred, while for the later case, there is issue with regards to safety as this could result to reactor run-away. Therefore, RDO was performed to design a system which is robust against uncertainties while having a reliable NH_3 production. This was done by maximizing the mean of the net NH_3 output flow rate while minimizing its standard deviation. With systems having optimized volume showing the highest temperature resilience, its corresponding direct and indirectly quenched systems were optimized.

Attempts on performing RDO on these systems were unsuccessful, mainly due to the solution not converging to a feasible design. It is believed that this is due to the combination of two things : definition of the constraints in the model, and the lowest value of the H_2/N_2 ratio considered during ramping. As explained in the methodology chapter, GEKKO solves the set of DAE by using Newton's method to iteratively find the solution within a feasible region, whose boundaries are defined by the constraints imposed in the model. These constraints were placed to specifically screen out impossible designs such as those with a mole fraction greater than 1, a molar flow rate which is negative, or a pressure which is negative. More importantly, because reactor run-away needs to be prevented, the highest temperature inside the reactor was limited to 900 K. Therefore, designs with temperatures greater 900 K inside the reactor were removed from the design space. On the other hand, the lowest value of the H_2/N_2 ratio considered during ramp-down is 1.31/2.69, which is adopted from Cheema et al.[20]. It is believed that for the reactor sizes considered here, this ratio might be too small. In the work of Cheema et al.[20], this value was reported as the minimum limit at which NH_3 production can still occur. However, their work makes use of volumes which are atleast 12 times smaller than the volumes considered in this thesis. Therefore, to operate at such a small ratio in larger reactors, the temperature inside the reactor needs to be very high, which is not possible due to the imposed constraints.

On the uncertainty propagation side, Mai et al. [78] demonstrated how the PCE failed to accurately represent the model a well-stirred, homogeneous chemical system which exhibited oscillatory response in species concentration due to uncertainties from its reaction parameters. To understand why PCE failed in this case, we need to discuss again how the PCE surrogate model is generated and validated. Consider a given sample set of size N which are inputs to the model. $N - 1$ points from this sample will be used to generate the surrogate model, while the excluded point x will be used for its validation. During validation, x will be used as input to both the actual and surrogate model, where the outcome obtained from the surrogate model will be compared to the one obtained from the actual model. If the difference between the outputs of two models are small enough (based on their LOO), then the surrogate model is considered representative of the actual model. In cases where a certain input causes an oscillatory response, the randomness of the oscillation's frequencies and amplitudes makes generation of a surrogate model capable of capturing these oscillations difficult.

Indeed, previous results in this thesis have shown that certain input variables bring the system to a certain limit of stable operation where ramping pushes the system to an unstable state, as manifested by the oscillations. Depending on which Hopf bifurcation point or fold bifurcation the system is in, the oscillations can be stable, characterized by constant amplitude and frequency, or unstable, characterized by dampening amplitudes towards a higher steady-state value or a lower steady-state value. Applied to this thesis, this implies that the inability of the surrogate model to capture these oscillations results to inaccurate mean and standard deviation values of the net NH_3 output flow rate. As both mean and standard deviation influences the population propagated by NSGA-II, the inconsistencies brought by the non-linear oscillatory response made convergence difficult to attain during optimization. To deal with this, the author [78] suggested to use time transformation to project the responses onto a suitable space, where a suitable warping can be chosen to minimize the difference in the frequency and phase between the surrogate and actual model. In doing so, the oscillatory response will be effectively captured by the surrogate model. Therefore, it is believed that the inability of the non time-warped PCE to capture these oscillatory response had also contributed to the failure of RDO. However, the main reason is perceived to be due to the chosen constraints and lowest H_2/N_2 ratio for the optimization.

Chapter 5

Conclusion

In this thesis, the dynamic simulation and optimization of an adiabatic, three-bed reactor system were made using GEKKO Python as the DAE solver. The NH_3 production capacities considered here were based from Thyssenkrupp's ammonia plant which was developed for power-to-ammonia applications. In this technology, renewable energy is used to power the electrolyzer which produces the H_2 needed for ammonia synthesis in the HBS loop. However, a fundamental issue lies with this set-up as the pre-existing HBS loop are not optimized for flexible operation. Therefore, optimization was performed under a scenario where the H_2/N_2 ratio was ramped to simulate the fluctuations in H_2 supply. Aside from the changes in H_2 supply, the resulting temperature changes inside the reactor is important as conditions might be reached where limit cycle behavior or reactor extinction occurs. These temperatures can be influenced by the reactor system's cooling configuration and amount of the catalyst. As such, the two most popular cooling configurations were studied, the direct and indirect quenching, where its effect on the temperature resilience was determined by comparing the most resilient and productive designs of both cooling configurations. These extreme designs were obtained from the multi-objective DDO which uses NSGA-II as the optimization algorithm. The RDO was then done by combining the NGSA-II with the PCE method for uncertainty quantification, to obtained designs with reliable NH_3 production.

The DDO step resulted to a Pareto front with its extreme ends corresponding to the most resilient and most productive design. The effect of cooling configuration on the resilience is mainly related to the possibility of the configuration to introduce less feed at the inlet without shutting down the system, and to maintain small temperature changes during ramping. In directly quenched system, the arrangement of distributing the feed into smaller fractions to comprise the inlet and quench streams, allow temperature changes to be well managed throughout ramping. While for indirectly quenched system, the arrangement of introducing the feed one time at the inlet calls for larger amounts of H_2 to be reacted, resulting to larger temperature changes which are more difficult to manage. As a result, the direct quenching configuration led to designs with the highest resilience. Meanwhile, the effect of reactor volume on resilience depends on the reactor system's cooling configuration. For the directly quenched system, there was no definitive influence of the reactor volume on resilience. That is, the resilience obtained was the same for both small and big reactors. On the other hand, the effect of reactor volume on resilience for the indirectly quenched system is limited to the last reactor bed, with smaller volumes leading to higher resilience. In deciding the best configuration under the scenario of fluctuating H_2 input, the indirectly quenched system was chosen due to its ability to exhibit high resilience without the limit cycle behavior, and high net NH_3 output flow rate due to higher residence times.

When studying the effect of uncertainties on the deterministic designs, worst-case scenarios comprising of the lowest and highest values of the uncertain parameters were implemented. At the lowest-value scenario, the combination led to an expected decrease in the outlet temperature, resulting to extinction during ramp-down. However, systems with optimized volumes showed recovery after ramping, with a decrease in resilience. At the highest-value scenario, the combination led to an expected increase in outlet temperatures allowing the system to either recover with a small decrease in temperature resilience or to transition to higher, steady-state temperature values after ramp-up. Finally, due to the constraint imposed in the RDO design and the H_2/N_2 ratio adopted for ramping, the RDO was unsuccessful.

Chapter 6

Future work

The greatest weakness of this thesis is the implementation of how resilience was calculated. Although the definition was adopted from Gong et al. [69], the resilience was calculated with reference to a lower-bound temperature value of zero. Because of this, despite achieving extinction, relatively high values of resilience were reported. This makes the reported resilience values not representative of the true performance of the reactor. In practice, once reactor extinction is achieved, the reactor is considered non-performing as it will then be subjected to special maintenance [57]. To address this, it is suggested that the lower-bound temperature value should be defined as the lowest temperature attained throughout ramping. Furthermore, the oscillations brought by the instability should be accounted for and avoided in the design, to avoid thermal cycling of the catalyst. The range of operation for which instability can be avoided is defined through a bifurcation study. When operating at non-deterministic conditions (highest-value case), high temperatures (at least 800 K) were obtained. Due to the higher heat capacity of the catalyst relative to the gas, the temperature difference between the two will become significant. As such, heterogeneous model should be adopted in the future. On the other hand, the RDO revealed that robustifying the system against uncertainties under very low H_2/N_2 ratio and limited reactor temperature range is not possible. To address this, it is suggested to study different ramping duration on the robustness of the design. Done this way, the flexibility of the design is further improved without depending on large H_2 storage tanks. It is also suggested to perform uncertainty quantification through time-warp PCE to allow the surrogate model to capture the oscillations in the response. Finally, inclusion of the entire HBS loop should be made, with regards to scheduling and cost optimization.

Appendix A

Bifurcation analysis from literature

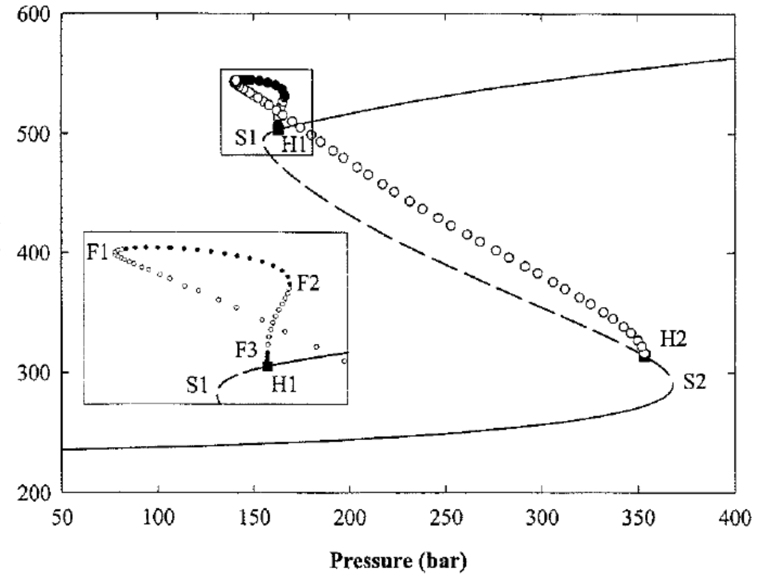

Figure A.1: The solution diagram of the bifurcation analysis done by Mancusi et al. [77], showing pressure as the bifurcation and temperature as the measured response. The solution can be divided into 4 types - (1) stable stationary solutions (solid lines), (2) unstable stationary solutions (dashed lines), (3) stable limit cycles (filled circles), and (4) unstable limit cycles (unfilled circles). The Hopf bifurcation (*H*) is the critical point of transition from steady-state behavior to limit cycle behavior, while the transition from the stable high conversion branch, 1, to the stable low conversion branch, 2, is defined by the fold bifurcations (*S*). Diagram taken from [77].

Bibliography

[1] Eric Martinot. “Grid Integration of Renewable Energy: Flexibility, Innovation, and Experience”. In: *Annual Review of Environment and Resources* 41 (2016), pp. 223–251. ISSN: 15435938. DOI: `10.1146/annurev-environ-110615-085725`.

[2] IEA ETSAP and IRENA. “Renewable Energy Integration in Power Grids. Technology Brief”. In: April (2015), pp. 1–36.

[3] European Commission. *Causes of climate change.* [Online; accessed 19-August-2021]. 2021. URL: `https://ec.europa.eu/clima/change/causes_en`.

[4] *Renewable energy targets.* [Online; accessed 19-August-2021]. 2021. URL: `https://ec.europa.eu/energy/topics/renewable-energy/directive-targets-and-rules/renewable-energy-targets_en`.

[5] *Renewable energy progress reports.* [Online; accessed 19-August-2021]. 2021. URL: `https://ec.europa.eu/energy/topics/renewable-energy/progress-reports_en`.

[6] Yasmina Bennani et al. “Power-to-Ammonia: Rethinking the role of ammonia – from a value product to a flexible energy carrier”. In: October 2015 (2016), pp. 1–110.

[7] Bruce N. Stram. “Key challenges to expanding renewable energy”. In: *Energy Policy* 96 (2016), pp. 728–734. ISSN: 03014215. DOI: `10.1016/j.enpol.2016.05.034`. URL: `http://dx.doi.org/10.1016/j.enpol.2016.05.034`.

[8] Da Xu et al. “Integrated Modelling and Enhanced Utilization of Power-to-Ammonia for High Renewable Penetrated Multi-Energy Systems”. In: *IEEE Transactions on Power Systems* 35.6 (2020), pp. 4769–4780. ISSN: 15580679. DOI: `10.1109/TPWRS.2020.2989533`.

[9] Eric Hsieh and Robert Anderson. “Grid flexibility: The quiet revolution”. In: *Electricity Journal* 30.2 (Feb. 2017). ISSN: 1040-6190. DOI: `10.1016/j.tej.2017.01.009`. URL: `https://www.osti.gov/biblio/1352338`.

[10] The European Wind Energy Association. *"Powering Europe", wind energy and the electricity grid*. Tech. rep. 1. 2012, pp. 48–67. DOI: `10.11333/jwea.36.1_48`.

[11] Kevin Verleysen et al. "How can power-to-ammonia be robust? Optimization of an ammonia synthesis plant powered by a wind turbine considering operational uncertainties". In: *Fuel* 266.December 2019 (2020), p. 117049. ISSN: 00162361. DOI: `10.1016/j.fuel.2020.117049`. URL: `https://doi.org/10.1016/j.fuel.2020.117049`.

[12] A. Valera-Medina et al. "Ammonia for power". In: *Progress in Energy and Combustion Science* 69 (2018), pp. 63–102. ISSN: 03601285. DOI: `10.1016/j.pecs.2018.07.001`. URL: `https://doi.org/10.1016/j.pecs.2018.07.001`.

[13] Wilkinson Siemens. "Siemens green Ammonia. 1st NH3 European event". In: *Netherlands: Rotterdam* (2017).

[14] Matthew J. Palys and Prodromos Daoutidis. "Using hydrogen and ammonia for renewable energy storage: A geographically comprehensive techno-economic study". In: *Computers and Chemical Engineering* 136 (2020), p. 106785. ISSN: 00981354. DOI: `10.1016/j.compchemeng.2020.106785`. URL: `https://doi.org/10.1016/j.compchemeng.2020.106785`.

[15] ISPT. "Power to Ammonia". In: *Report* (2017). URL: `http://www.ispt.eu/media/ISPT-P2A-Final-Report.pdf`.

[16] Matthias Bohnet. *Ullmann's encyclopedia of industrial chemistry*. Wiley-Vch, 2003.

[17] S. Giddey, S. P.S. Badwal, and A. Kulkarni. "Review of electrochemical ammonia production technologies and materials". In: *International Journal of Hydrogen Energy* 38.34 (2013), pp. 14576–14594. ISSN: 03603199. DOI: `10.1016/j.ijhydene.2013.09.054`. URL: `http://dx.doi.org/10.1016/j.ijhydene.2013.09.054`.

[18] Arif Karabeyoglu and Brian Evans. "Fuel Conditioning System for Ammonia-Fired Power Plants". In: 9th Annual NH3 Fuel Association Conference (San Antonio, Texas). 2012.

[19] J Eichman, K Harrison, and M Peters. *Novel Electrolyzer Applications : Providing More Than Just Hydrogen*. Tech. rep. September. National Renewable Energy Laboratory, 2014, pp. 1–24. URL: `http://www.nrel.gov/docs/fy14osti/61758.pdf`.

[20] Izzat Iqbal Cheema and Ulrike Krewer. "Optimisation of the Autothermal NH3 Production Process for Power-to-Ammonia". In: *Processes* 8.1 (2019), p. 38. ISSN: 2227-9717. DOI: `10.3390/pr8010038`.

[21] Lu Wang et al. “Greening Ammonia toward the Solar Ammonia Refinery”. In: *Joule* 2.6 (2018), pp. 1055–1074. ISSN: 25424351. DOI: `10.1016/j.joule.2018.04.017`. URL: `https://doi.org/10.1016/j.joule.2018.04.017`.

[22] Jan Willem Erisman et al. “How a century of ammonia synthesis changed the world”. In: *Nature Geoscience* 1.10 (2008), pp. 636–639. ISSN: 17520894. DOI: `10.1038/ngeo325`.

[23] Robert Steinberger-Wilckens and Beatrice Sampson. “Chapter 8 - Market, Commercialization, and Deployment—Toward Appreciating Total Owner Cost of Hydrogen Energy Technologies”. In: *Science and Engineering of Hydrogen-Based Energy Technologies*. Ed. by Paulo Emilio V de Miranda. Academic Press, 2019, pp. 383–403. ISBN: 978-0-12-814251-6. DOI: `https://doi.org/10.1016/B978-0-12-814251-6.00008-3`. URL: `http://www.sciencedirect.com/science/article/pii/B9780128142516000083`.

[24] Collin Smith, Alfred K. Hill, and Laura Torrente-Murciano. “Current and future role of Haber-Bosch ammonia in a carbon-free energy landscape”. In: *Energy and Environmental Science* 13.2 (2020), pp. 331–344. ISSN: 17545706. DOI: `10.1039/c9ee02873k`.

[25] Deepak K. Ojha et al. “Integrated Ammonia Synthesis and Separation”. In: *ACS Sustainable Chemistry and Engineering* 7.23 (2019), pp. 18785–18792. ISSN: 21680485. DOI: `10.1021/acssuschemeng.9b03050`.

[26] Muhammad Aziz et al. “Combined nitrogen production, ammonia synthesis, and power generation for efficient hydrogen storage”. In: *Energy Procedia* 143 (2017), pp. 674–679. ISSN: 18766102. DOI: `10.1016/j.egypro.2017.12.745`. URL: `https://doi.org/10.1016/j.egypro.2017.12.745`.

[27] Michael Reese et al. “Performance of a Small-Scale Haber Process”. In: *Industrial and Engineering Chemistry Research* 55.13 (2016), pp. 3742–3750. ISSN: 15205045. DOI: `10.1021/acs.iecr.5b04909`.

[28] Masayasu Nishi, Shih-Yuan Chen, and Hideyuki Takagi. “Mild Ammonia Synthesis over Ba-Promoted Ru/MPC Catalysts: Effects of the Ba/Ru Ratio and the Mesoporous Structure”. In: *Catalysts* 9.5 (2019). ISSN: 2073-4344. DOI: `10.3390/catal9050480`. URL: `https://www.mdpi.com/2073-4344/9/5/480`.

[29] Michael A. Shipman and Mark D. Symes. “Recent progress towards the electrosynthesis of ammonia from sustainable resources”. In: *Catalysis Today* 286 (2017), pp. 57–68. ISSN: 09205861. DOI: `10.1016/j.cattod.2016.05.008`. URL: `http://dx.doi.org/10.1016/j.cattod.2016.05.008`.

[30] Gerhard Ertl. *Nobel lecture on reactions at surfaces: fro atoms to complexity*. [Online; accessed 27-December-2020]. 2007.

[31] Si-Jia Li et al. “Amorphizing of Au Nanoparticles by CeOx–RGO Hybrid Support towards Highly Efficient Electrocatalyst for N2 Reduction under Ambient Conditions”. In: *Advanced Materials* 29.33 (2017), p. 1700001. DOI: `https://doi.org/10.1002/adma.201700001`. eprint: `https://onlinelibrary.wiley.com/doi/pdf/10.1002/adma.201700001`. URL: `https://onlinelibrary.wiley.com/doi/abs/10.1002/adma.201700001`.

[32] Gilbert F. Froment, Kenneth B. Bischoff, and Juray De Wilde. *Chemical Reactor Analysis and Design*. 3rd ed. John Wiley & Sons, Inc., 2011, p. 634. ISBN: 9783540773405.

[33] Mohammad Hasan Khademi and Reyhaneh Sadat Sabbaghi. “Comparison between three types of ammonia synthesis reactor configurations in terms of cooling methods”. In: *Chemical Engineering Research and Design* 128 (2017), pp. 306–317. ISSN: 02638762. DOI: `10.1016/j.cherd.2017.10.021`. URL: `http://dx.doi.org/10.1016/j.cherd.2017.10.021`.

[34] Thyssenkrup. *Ammonia technology.* [Online; accessed 13-October-2020]. 2018. URL: `https://ucpcdn.thyssenkrupp.com/_legacy/UCPthyssenkruppBAIS/assets.files/products___services/fertilizer_plants/ammonium_sulphate_plants/brochure-ammonia_scr.pdf`.

[35] Gerard B. Hawkings. *Ammonia Synthesis Flowsheet Operator Training.* [Online; accessed 13-October-2020]. URL: `https://www.slideshare.net/GerardBHawkins/ammonia-synthesis-flowsheet-operator-training`.

[36] Izzat Iqbal Cheema and Ulrike Krewer. “Operating envelope of Haber-Bosch process design for power-to-ammonia”. In: *RSC Advances* 8.61 (2018), pp. 34926–34936. ISSN: 20462069. DOI: `10.1039/c8ra06821f`.

[37] Dohyung Kim et al. “Artificial Photosynthesis for Sustainable Fuel and Chemical Production”. In: *Angewandte Chemie International Edition* 54.11 (2015), pp. 3259–3266. DOI: `https://doi.org/10.1002/anie.201409116`. URL: `https://onlinelibrary.wiley.com/doi/abs/10.1002/anie.201409116`.

[38] Rong Lan, John T.S. Irvine, and Shanwen Tao. “Synthesis of ammonia directly from air and water at ambient temperature and pressure”. In: *Scientific Reports* 3 (2013), pp. 1–7. ISSN: 20452322. DOI: `10.1038/srep01145`.

[39] Chengcheng Li, Tuo Wang, and Jinlong Gong. “Alternative Strategies Toward Sustainable Ammonia Synthesis”. In: *Transactions of Tianjin University* 26.2 (2020), pp. 67–91. ISSN: 19958196. DOI: `10.1007/s12209-020-00243-x`. URL: `https://doi.org/10.1007/s12209-020-00243-x`.

[40] Ioannis Garagounis et al. *Electrochemical synthesis of ammonia: Recent efforts and future outlook.* 2019. DOI: `10.3390/membranes9090112`. URL: `www.mdpi.com/journal/membranes`.

[41] Tingting Wu et al. "Electrochemical Synthesis of Ammonia: Progress and Challenges". In: *Materials Today Physics* 16 (2020), p. 100310. ISSN: 25425293. DOI: `10.1016/j.mtphys.2020.100310`. URL: `https://doi.org/10.1016/j.mtphys.2020.100310`.

[42] V. Kyriakou et al. "Progress in the Electrochemical Synthesis of Ammonia". In: *Catalysis Today* 286 (2017), pp. 2–13. ISSN: 09205861. DOI: `10.1016/j.cattod.2016.06.014`. URL: `http://dx.doi.org/10.1016/j.cattod.2016.06.014`.

[43] B.S. Patil et al. "Plasma N2-fixation : 1900-2014". English. In: *Catalysis Today* 256.1 (2015), pp. 49–66. ISSN: 0920-5861. DOI: `10.1016/j.cattod.2015.05.005`.

[44] Kr. Birkeland. "On the oxidation of atmospheric nitrogen in electric arcs". In: *Trans. Faraday Soc.* 2.December (1906), pp. 98–116. DOI: `10.1039/TF9060200098`. URL: `http://dx.doi.org/10.1039/TF9060200098`.

[45] Annemie Bogaerts and Erik C. Neyts. "Plasma Technology: An Emerging Technology for Energy Storage". In: *ACS Energy Letters* 3.4 (2018), pp. 1013–1027. ISSN: 23808195. DOI: `10.1021/acsenergylett.8b00184`.

[46] Peng Peng et al. "A review on the non-thermal plasma-assisted ammonia synthesis technologies". In: *Journal of Cleaner Production* 177 (2018), pp. 597–609. ISSN: 09596526. DOI: `10.1016/j.jclepro.2017.12.229`. URL: `https://doi.org/10.1016/j.jclepro.2017.12.229`.

[47] Peng Peng et al. "Atmospheric Pressure Ammonia Synthesis Using Non-thermal Plasma Assisted Catalysis". In: *Plasma Chemistry and Plasma Processing* 36.5 (2016), pp. 1201–1210. ISSN: 02724324. DOI: `10.1007/s11090-016-9713-6`.

[48] N. Cherkasov, A. O. Ibhadon, and P. Fitzpatrick. "A review of the existing and alternative methods for greener nitrogen fixation". In: *Chemical Engineering and Processing: Process Intensification* 90 (2015), pp. 24–33. ISSN: 02552701. DOI: `10.1016/j.cep.2015.02.004`. URL: `http://dx.doi.org/10.1016/j.cep.2015.02.004`.

[49] Annemie Bogaerts et al. "The 2020 plasma catalysis roadmap". In: *Journal of Physics D: Applied Physics* 53.44 (2020). ISSN: 13616463. DOI: `10.1088/1361-6463/ab9048`.

[50] Ulrich Kogelschatz. “Dielectric-Barrier Discharges: Their History, Discharge Physics, and Industrial Applications”. In: *Plasma Chemistry and Plasma Processing* 23.1 (2003), pp. 1–46. ISSN: 1572-8986. DOI: `10.1023/A:1022470901385`. URL: `https://doi.org/10.1023/A:1022470901385`.

[51] Murielle Schreck and Markus Niederberger. “Photocatalytic Gas Phase Reactions”. In: *Chemistry of Materials* 31.3 (2019), pp. 597–618. ISSN: 15205002. DOI: `10.1021/acs.chemmater.8b04444`.

[52] Shuai Zhang et al. “Photocatalytic ammonia synthesis: Recent progress and future”. In: *EnergyChem* 1.2 (2019), p. 100013. ISSN: 25897780. DOI: `10.1016/j.enchem.2019.100013`. URL: `https://doi.org/10.1016/j.enchem.2019.100013`.

[53] Manh Hiep Vu, M. Sakar, and Trong On Do. “Insights into the recent progress and advanced materials for photocatalytic nitrogen fixation for ammonia (NH 3) production”. In: *Catalysts* 8.12 (2018). ISSN: 20734344. DOI: `10.3390/catal8120621`.

[54] Hyun Ha Kim et al. “Plasma Catalysis for Environmental Treatment and Energy Applications”. In: *Plasma Chemistry and Plasma Processing* 36.1 (2016), pp. 45–72. ISSN: 02724324. DOI: `10.1007/s11090-015-9652-7`.

[55] Galip Akay and Kui Zhang. “Process Intensification in Ammonia Synthesis Using Novel Coassembled Supported Microporous Catalysts Promoted by Nonthermal Plasma”. In: *Industrial & Engineering Chemistry Research* 56.2 (2017), pp. 457–468. ISSN: 0888-5885. DOI: `10.1021/acs.iecr.6b02053`. URL: `https://doi.org/10.1021/acs.iecr.6b02053`.

[56] S. Schulte Beerbühl, M. Fröhling, and F. Schultmann. “Combined scheduling and capacity planning of electricity-based ammonia production to integrate renewable energies”. In: *European Journal of Operational Research* 241.3 (2015), pp. 851–862. ISSN: 03772217. DOI: `10.1016/j.ejor.2014.08.039`.

[57] John C. Morud and Sigurd Skogestad. “Analysis of Instability in an Industrial Ammonia Reactor”. In: *AIChE Journal* 44.4 (1998), pp. 888–895. ISSN: 00011541. DOI: `10.1002/aic.690440414`.

[58] Rebecca Maria Brigitte Gullberg, Vidar Alstad, and Yara International ASA. “Controllability Analysis of Ammonia Synthesis Loops”. MA thesis. Norwegian University of Science and Technology, 2018.

[59] D. C. Dyson and J. M. Simon. “A kinetic expression with diffusion correction for ammonia synthesis on industrial catalyst”. In: *Industrial and Engineering Chemistry Fundamentals* 7.4 (1968), pp. 605–610. ISSN: 01964313. DOI: `10.1021/i160028a013`.

[60] S. S.E.H. Elnashaie and F. M. Alhabdan. “A computer software package for the simulation and optimization of an industrial ammonia converter based on a rigorous heterogeneous model”. In: *Mathematical and Computer Modelling* 12.12 (1989), pp. 1589–1600. ISSN: 08957177. DOI: `10.1016/0895-7177(89)90335-X`.

[61] Maurizio Rovaglio, Davide Manca, and Francesco Cortese. “A reliable control for the ammonia loop facing limit-cycle and snowball effects”. In: *AIChE Journal* 50.6 (2004), pp. 1229–1241. ISSN: 00011541. DOI: `10.1002/aic.10103`.

[62] Leroy Chiao and Robert G. Rinker. “On the Use of Approximations in the Modelling of Plug-Flow Reactors Under Periodic Operation”. In: *Chemical Engineering Communications* 57.1-6 (1987), pp. 153–165. ISSN: 15635201. DOI: `10.1080/00986448708960482`.

[63] T.L. Bergman et al. *Introduction to Heat Transfer*. Wiley, 2011. ISBN: 9780470501962. URL: `https://books.google.be/books?id=YBaNaLurTD4C`.

[64] Logan D.R. Beal et al. “GEKKO optimization suite”. In: *Processes* 6.8 (2018). ISSN: 22279717. DOI: `10.3390/pr6080106`.

[65] Jorge Nocedal, Andreas Wächter, and Richard A. Waltz. “Adaptive barrier update strategies for nonlinear interior methods”. In: *SIAM Journal on Optimization* 19.4 (2008), pp. 1674–1693. ISSN: 10526234. DOI: `10.1137/060649513`.

[66] Joel A E Andersson et al. “CasADi – A software framework for nonlinear optimization and optimal control”. In: *Mathematical Programming Computation* 11.1 (2019), pp. 1–36. DOI: `10.1007/s12532-018-0139-4`.

[67] Rhys Tucker and Karan Bagga. *From Micro to Mega How the green ammonia concept adapts*. [Online; accessed 1-June-2021]. 2019. URL: `https://www.ammoniaenergy.org/wp-content/uploads/2021/06/4.2-tkIS-Micro-to-Mega-Ammonia-plants.pdf`.

[68] Julien Armijo and Cédric Philibert. “Flexible production of green hydrogen and ammonia from variable solar and wind energy: Case study of Chile and Argentina”. In: *International Journal of Hydrogen Energy* 45.3 (2020), pp. 1541–1558. ISSN: 03603199. DOI: `10.1016/j.ijhydene.2019.11.028`.

[69] Jian Gong and Fengqi You. “Resilient design and operations of process systems: Nonlinear adaptive robust optimization model and algorithm for resilience analysis and enhancement”. In: *Computers and Chemical Engineering* 116 (2018), pp. 231–252. ISSN: 00981354. DOI: `10.1016/j.compchemeng.2017.11.002`. URL: `https://doi.org/10.1016/j.compchemeng.2017.11.002`.

[70] Akira Murase, Howard Roberts, and Alvin Converse. "Optimal Thermal Design". In: *Industrial Engineering Chemistry Process Design and Development* 9.4 (1970), pp. 503 –513.

[71] P. Tsirikoglou and D. Coppitters. "Robust design optimization of renewable Hydrogen and dErIved energy cArrier systems framework (RHEIA)". In: (2020). URL: `https://rheia.readthedocs.io/en/latest/index.html`.

[72] Kevin Verleysen, Alessandro Parente, and Francesco Contino. "How sensitive is a dynamic ammonia synthesis process? Global sensitivity analysis of a dynamic Haber-Bosch process (for flexible seasonal energy storage)". In: *Energy* 232 (2021), p. 121016. ISSN: 03605442. DOI: `10.1016/j.energy.2021.121016`. URL: `https://doi.org/10.1016/j.energy.2021.121016`.

[73] P. Laššák, J. Labovský, and Ĺ Jelemenský. "Influence of parameter uncertainty on modeling of industrial ammonia reactor for safety and operability analysis". In: *Journal of Loss Prevention in the Process Industries* 23.2 (2010), pp. 280–288. ISSN: 09504230. DOI: `10.1016/j.jlp.2009.10.001`.

[74] N Srinivas and Kalyanmoy Deb. "Multiobjective Function Optimization Using Nondominated Sorting Genetic Algorithms". In: *Evolutionary Computation* 2.3 (2000), pp. 221–248.

[75] Kalyanmoy Deb et al. "A fast and elitist multiobjective genetic algorithm: NSGA-II". In: *IEEE Transactions on Evolutionary Computation* 6.2 (2002), pp. 182–197. ISSN: 1089778X. DOI: `10.1109/4235.996017`.

[76] Bruno Sudret. *Risk and Reliability in Geotechnical Engineering.* Ed. by Kok-Kwang Phoon and Jianye Ching. December 2014. CRC Press, 2014. Chap. Polynomial chaos expansions and stochastic finite element methods, pp. 265–300. ISBN: 9781482227215.

[77] E. Mancusi et al. "Multistability and hysteresis in an industrial ammonia reactor". In: *AIChE Journal* 46.4 (2000), pp. 824–828. ISSN: 00011541. DOI: `10.1002/aic.690460415`.

[78] Chu V. Mai and Bruno Sudret. "Surrogate models for oscillatory systems using sparse polynomial chaos expansions and stochastic time warping". In: *SIAM-ASA Journal on Uncertainty Quantification* 5.1 (2017), pp. 540–571. ISSN: 21662525. DOI: `10.1137/16M1083621`. arXiv: `1609.09286`.

UNIVERSITÉ CATHOLIQUE DE LOUVAIN
École polytechnique de Louvain
Rue Archimède, 1 bte L6.11.01, 1348 Louvain-la-Neuve, Belgique | **www.uclouvain.be/epl**